Electronic Supplementary Material (ESI) for Energy & Environmental Science

Supporting Information

Phase reconfiguration of multivalent nickel sulfides in hydrogen evolution

Yu Sun,[a,b,c] Jing Wu,[a,b,c] Zheng Zhang,[a,b,c] Qingliang Liao,[a,b] Suicai Zhang,[a,b] Xin Wang,[a,b] Yong Xie,[a,b] Kaikai Ma,[a,b] Zhuo Kang*[a,b] and Yue Zhang*[a,b]

[a]Beijing Advanced Innovation Center for Materials Genome Engineering, Beijing Key Laboratory for Advanced Energy Materials and Technologies, University of Science and Technology Beijing, Beijing 100083, China

[b]State Key Laboratory for Advanced Metals and Materials, School of Materials Science and Engineering, University of Science and Technology Beijing, Beijing 100083, China

[c]These authors contributed equally: Yu Sun, Jing Wu, Zheng Zhang.

*e-mail: zhuokang@ustb.edu.cn; yuezhang@ustb.edu.cn

Supporting Figures

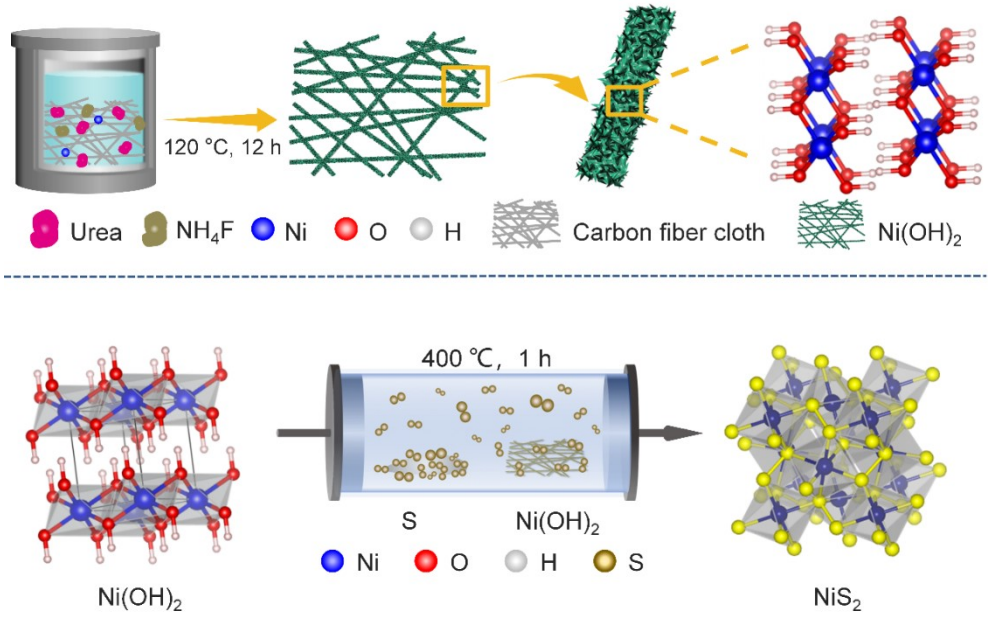

Figure S1. Fabrication of $Ni_{1-x}Fe_xS_2$ catalysts. Schematic illustration of the fabrication procedure by directly growing $Ni_{1-x}Fe_xS_2$ NSs, and the sulfurization process at 400 ℃ under the Argon protection.

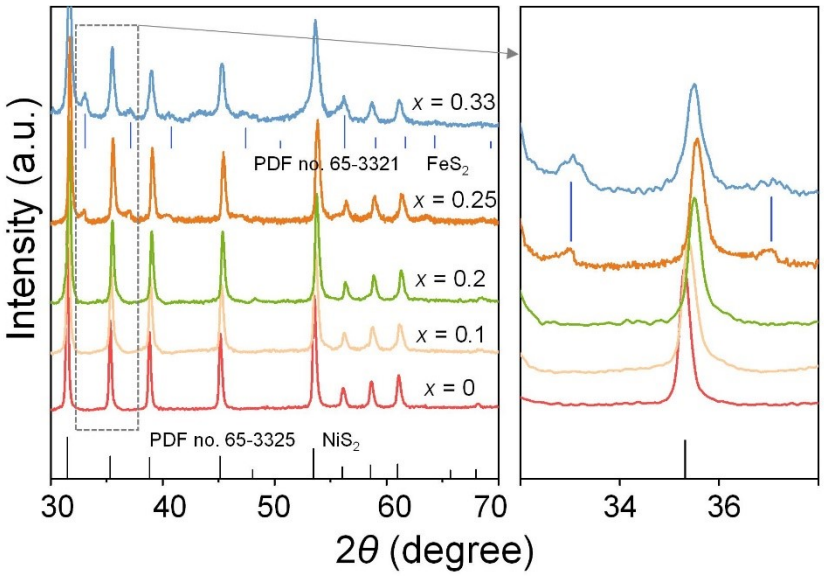

Figure S2. PXRD patterns of synthesized $Ni_{1-x}Fe_xS_2$ ($x \approx$ 0-0.33). The right axis show the unit cell of cubic metal disulfides and the magnified PXRD patterns in the range between 32 and 38.

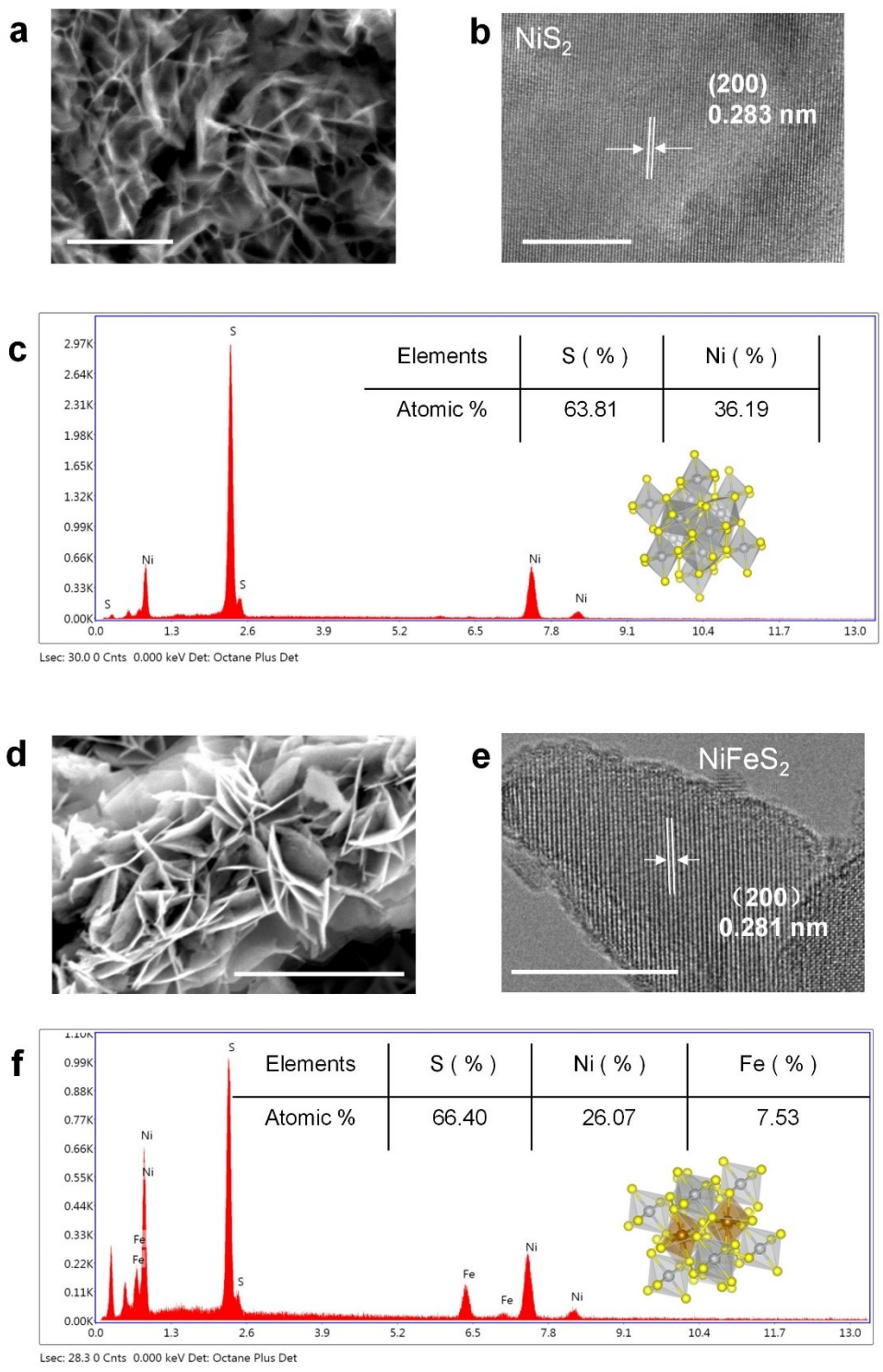

Figure S3. SEM-EDS elemental analysis and the TEM images of the as-prepared $Ni_{1-x}Fe_xS_2$ electrode. **a**, SEM images of the carbon fiber coated with NiS_2. Scale bar, 1 μm. **b**, TEM images of NiS_2 NSs. Scale bar, 5 nm. **c**, The corresponding EDS elemental atomic ratio of Ni and S elements. **d**, Top-view SEM images of the carbon fiber coated with $Ni_{0.8}Fe_{0.2}S_2$ NSs. Scale bar, 10 μm. **e**, TEM images of $Ni_{0.8}Fe_{0.2}S_2$ NSs. Scale bar, 10 nm. **f**, The corresponding EDS elemental atomic ratio of Ni, Fe and S elements. Insets of (**c**) and (**f**) is the corresponding atomic ratio of Ni, Fe and S elements and the lattice structure of $Ni_{1-x}Fe_xS_2$.

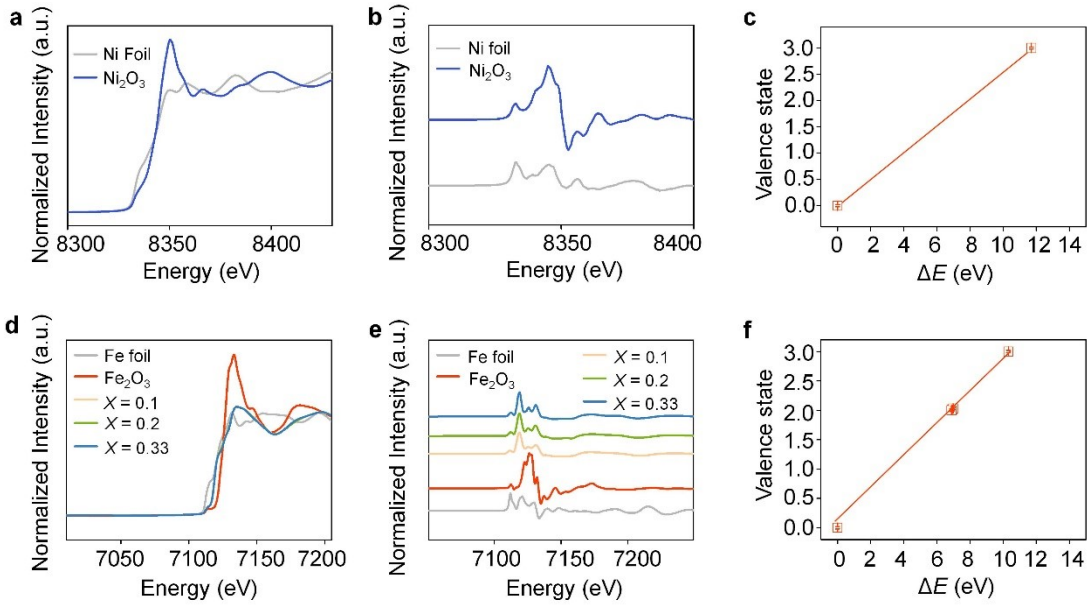

Figure S4. XAFS measurements. **a**, XANES spectra recorded at the Ni K-edge of nickel foil and Ni_2O_3. **b**, Normalized difference spectra for Ni K-edge XANES. **c**, The fitted average valence states of Ni from XANES spectra. Valence state of Ni Foil is approximately close to 0, valence state of Ni_2O_3 is approximately close to 3+. **d**, XANES spectra recorded at the Fe K-edge of Iron foil and Fe_2O_3. **e**, Normalized difference spectra for Fe K-edge XANES. **f**, The fitted average valence states of Fe from XANES spectra. Valence state of Fe Foil is approximately close to 0, valence state of Fe_2O_3 is approximately close to 3+. Error bars represent the standard deviation from at least three independent measurements.

Ni and Fe valence states of the samples were estimated by means of the absorption edge energy E_0, which was defined as the energy at the highest first derivative of the absorbance as shown in Figure S4b, e. Correspondingly, the absorption edge energy E_0 of Ni foil with Ni^0 valence state is determined as 8333.00 eV. Similarly, the Ni K-edge EXAFS spectra showed that the absorption edge energies E_0 of the NiS_2, $Ni_{0.9}Fe_{0.1}S_2$, $Ni_{0.8}Fe_{0.2}S_2$, and $Ni_{0.67}Fe_{0.33}S_2$ and Ni_2O_3 were located at 8360.68, 8340.35, 8340.12, and 8340.27 and 8344.61 eV, respectively. The Fe K-edge EXAFS spectra presented that the absorption edge energies E_0 of the Fe Foil, $Ni_{0.9}Fe_{0.1}S_2$, $Ni_{0.8}Fe_{0.2}S_2$, and $Ni_{0.67}Fe_{0.33}S_2$ and Fe_2O_3 were located at 7112, 7118.92, 7118.98, 7118.89 and 7122.32 eV, respectively.

The obtained energy shifts (ΔE), as a function of the valence state, were shown in Figure S4c, f, together with a model linear function, which have been determined as a best fit to the data from the reference samples. Nickel and iron valence states in the synthesized Fe substituted nickel sulfides were calculated from the linear function, and these data were listed in Table S1.

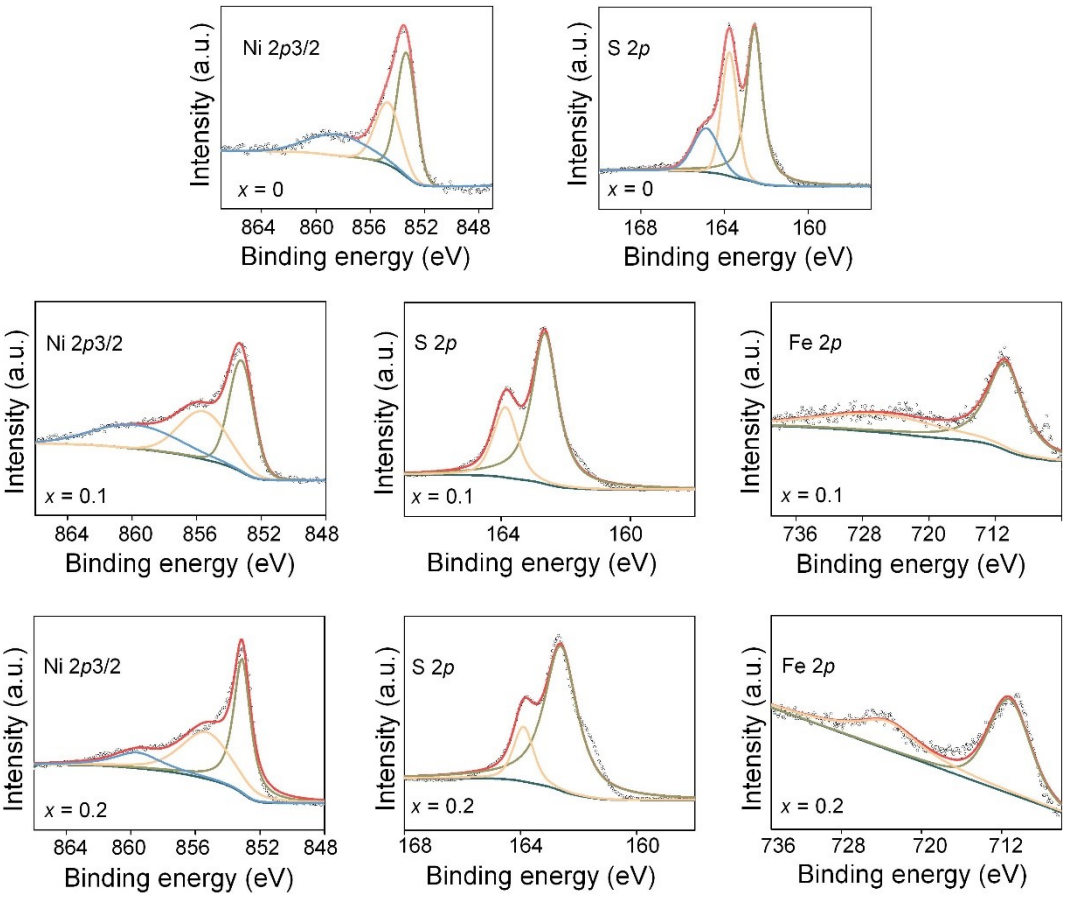

Figure S5. XPS Characterization of $Ni_{1-x}Fe_xS_2$ (x = 0, 0.1, 0.2) for the Ni 2*p*3/2, S 2*p* and Fe 2*p* regions. The broad S 2*p* XPS peak was fitted into two main peaks. The peaks located at 162.6 and 163.8 eV were attributed to the S 2*p*3/2 and S 2*p*1/2 orbitals of bridging S_2^{2-}.

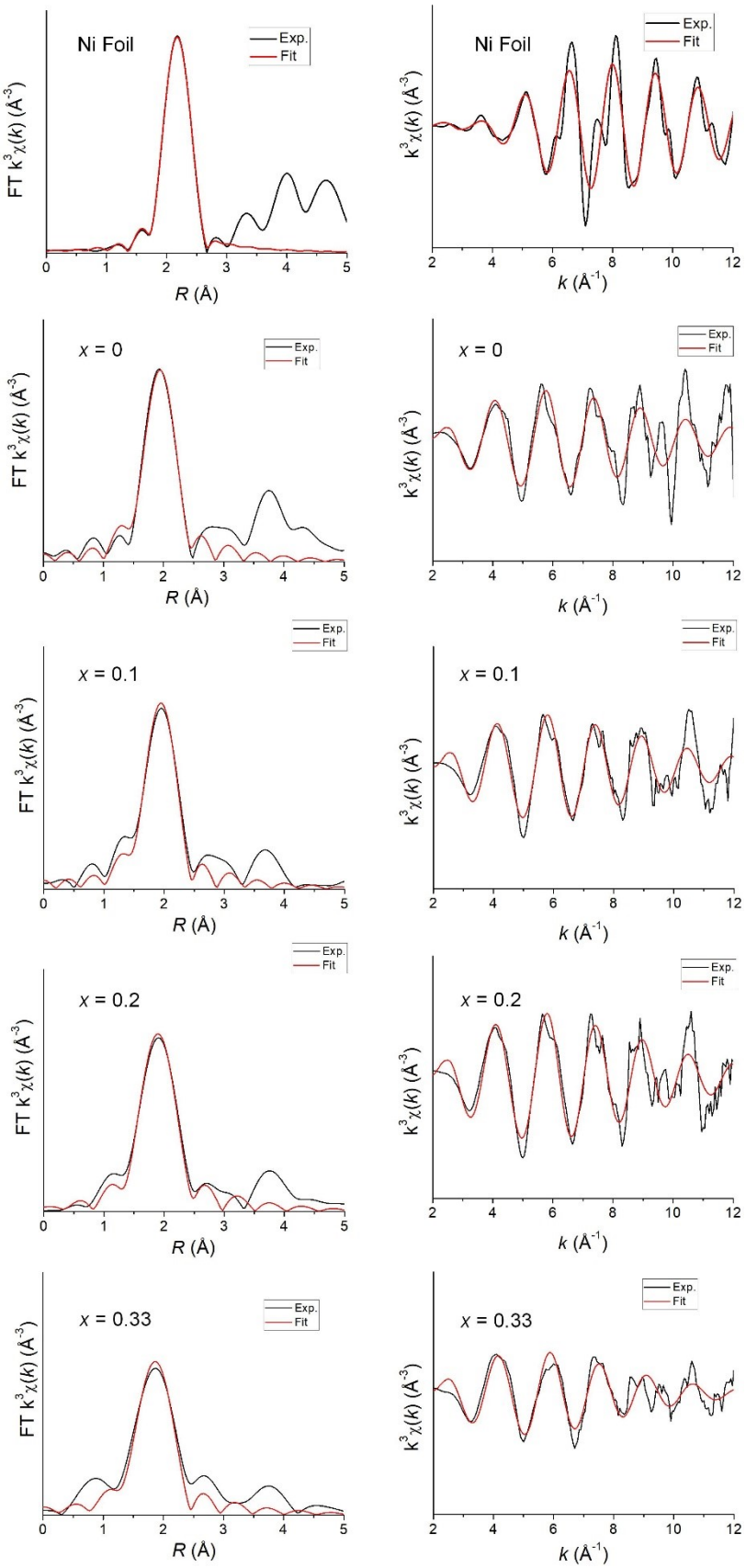

Figure S6. Ni K-edge EXAFS analysis of samples in *R* and *k* spaces. FT-EXAFS spectra and fits of Ni K-edges from Ni foil and $Ni_{1-x}Fe_xS_2$ (x = 0, 0.1, 0.2, 0.33) catalysts. The black lines represent the experiment data and the red lines represent the fitting values.

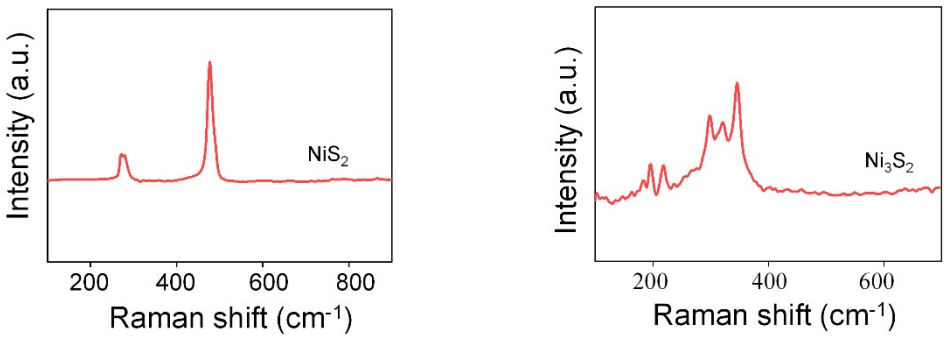

Figure S7. Raman spectrum of NiS_2 and Ni_3S_2. The peaks at 274.4(T_g), 284.8(E_g), 479.3(A_g) cm^{-1} previously attributed to NiS_2, peaks at 187.6 (A_1(2)), 202.1 (E(4)), 223.6 (E(3)), 303.6 (E(2)), 324.6 (A_1(1)), 350.3 (E(1)) cm^{-1} were correlated respectively with two A_1 stretching and four E bending vibration of Ni-S in the heazlewoodite-phase Ni_3S_2, and the peaks were shown in Table S4.

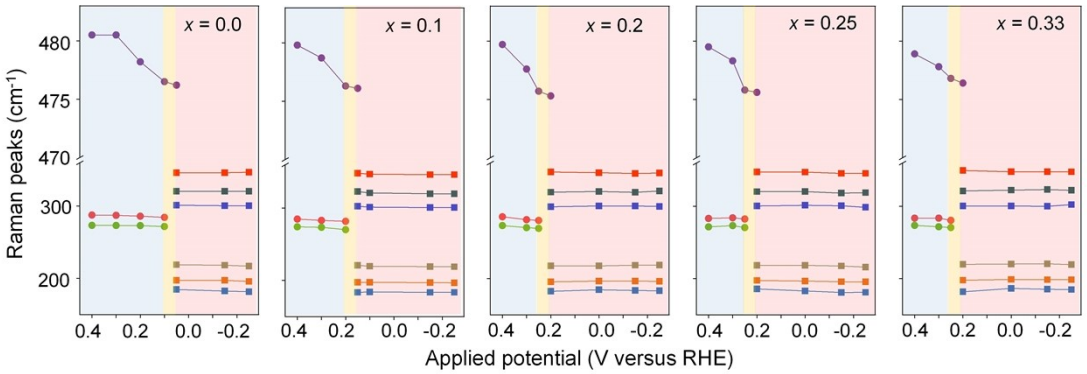

Figure S8. Frequency of the vibrational modes versus the applied potential obtained from the in-situ Raman spectra for $Ni_{1-x}Fe_xS_2$.

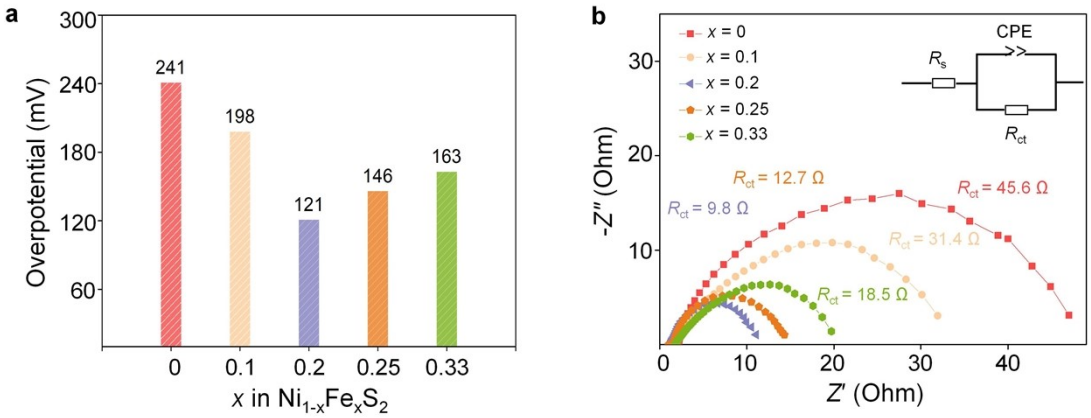

Figure S9. Electrochemical characterization of $Ni_{1-x}Fe_xS_2$. **a**, Overpotential of the nickel sulfide catalysts at the current density of 10 $mAcm^{-2}$, **b**, Nyquist plots of the catalyst electrode @150 mV overpotential in 1M KOH. Inset of (**b**) is the simplified Randles equivalent circuit model. The intercept in the high frequency zone is attributed to the internal charge-transfer resistances or the system resistance (R_s) of electrodes, and the semicircles represent the charge transfer resistances (R_{ct}) at the electrode/electrolyte interface. The charge-transfer resistances (R_{ct}) measured at 150 mV overpotential are 45.6, 31.4, 9.8, 12.7 and 18.5 Ω for the CFP-supported pure NiS_2, $Ni_{0.9}Fe_{0.1}S_2$, $Ni_{0.8}Fe_{0.2}S_2$, $Ni_{0.75}Fe_{0.25}S_2$ and $Ni_{0.67}$ $Fe_{0.33}S_2$, respectively.

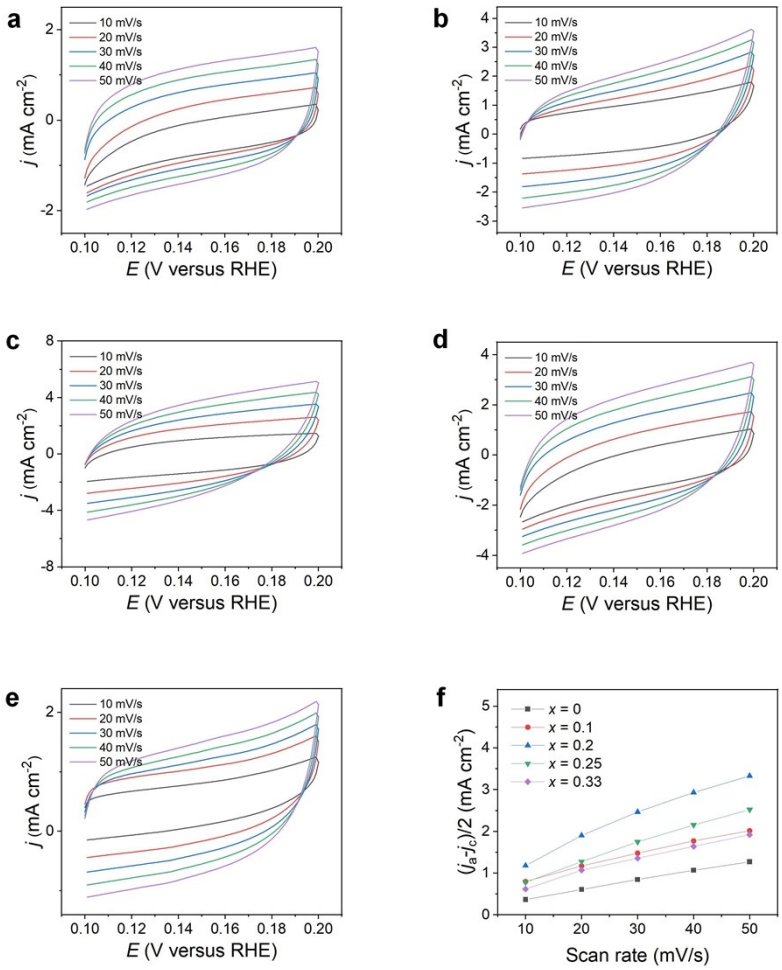

Figure S10. Cyclic voltammograms in the non-Faradaic potential region (0.1 to 0.2 V versus RHE) for the $Ni_{1-x}Fe_xS_2$ (**a**, $x = 0$; **b**, $x = 0.1$; **c**, $x = 0.2$; **d**, $x = 0.25$; **e**, $x = 0.33$) catalysts at different scan rates (10, 20, 30, 40, 50 mV s^{-1}). **f**, Charging current density differences at 0.15 V versus RHE plotted against scan rate. The value of C_{dl} was estimated from the slope of the linear relationship between the half capacitive current density ($(j_{anodic} - j_{cathodic})/2$) at the middle of the applied potential range and the scan rates. Significantly, $Ni_{0.8}Fe_{0.2}S_2$ yielded an extremely high C_{dl} value up to 53.28 mF cm^{-2}, considerably larger than those of the NiS_2 (22.7 mF cm^{-2}), $Ni_{0.9}Fe_{0.1}S_2$ (30.38 mF cm^{-2}), $Ni_{0.75}Fe_{0.25}S_2$ (43.59 mF cm^{-2}) and $Ni_{0.67}Fe_{0.33}S_2$ (34.7 mF cm^{-2}).

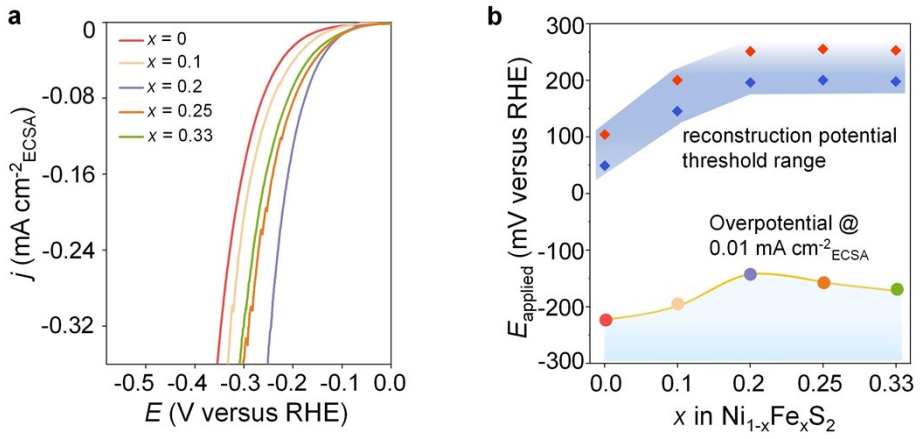

Figure S11. a, Normalized specific activities by ECSAs of various $Ni_{1-x}Fe_xS_2$ catalysts. **b**, the surface reconstruction potential threshold range for $Ni_{1-x}Fe_xS_2$ samples, and the corresponding intrinsic activity extracted from ECSA (overpotentials@0.01 $mAcm^{-2}_{ECSA}$) of hydrogen evolution are plotted to show the dynamic correlation of structure-activity.

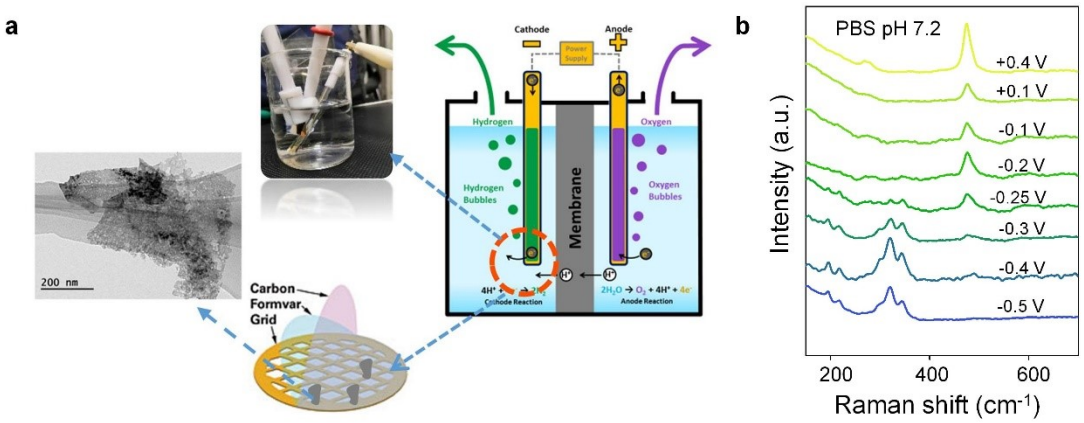

Figure S12. TEM characterization of surface-restructured nickel sulfide after the process of HER. **a**, Schematic process of HRTEM of nickel sulfide. **b**, In-situ Raman spectra of NiS_2 at the potentials of 0.4 V~-0.5 V (vs. RHE) in 0.01M PBS (NaPi, pH7.2).

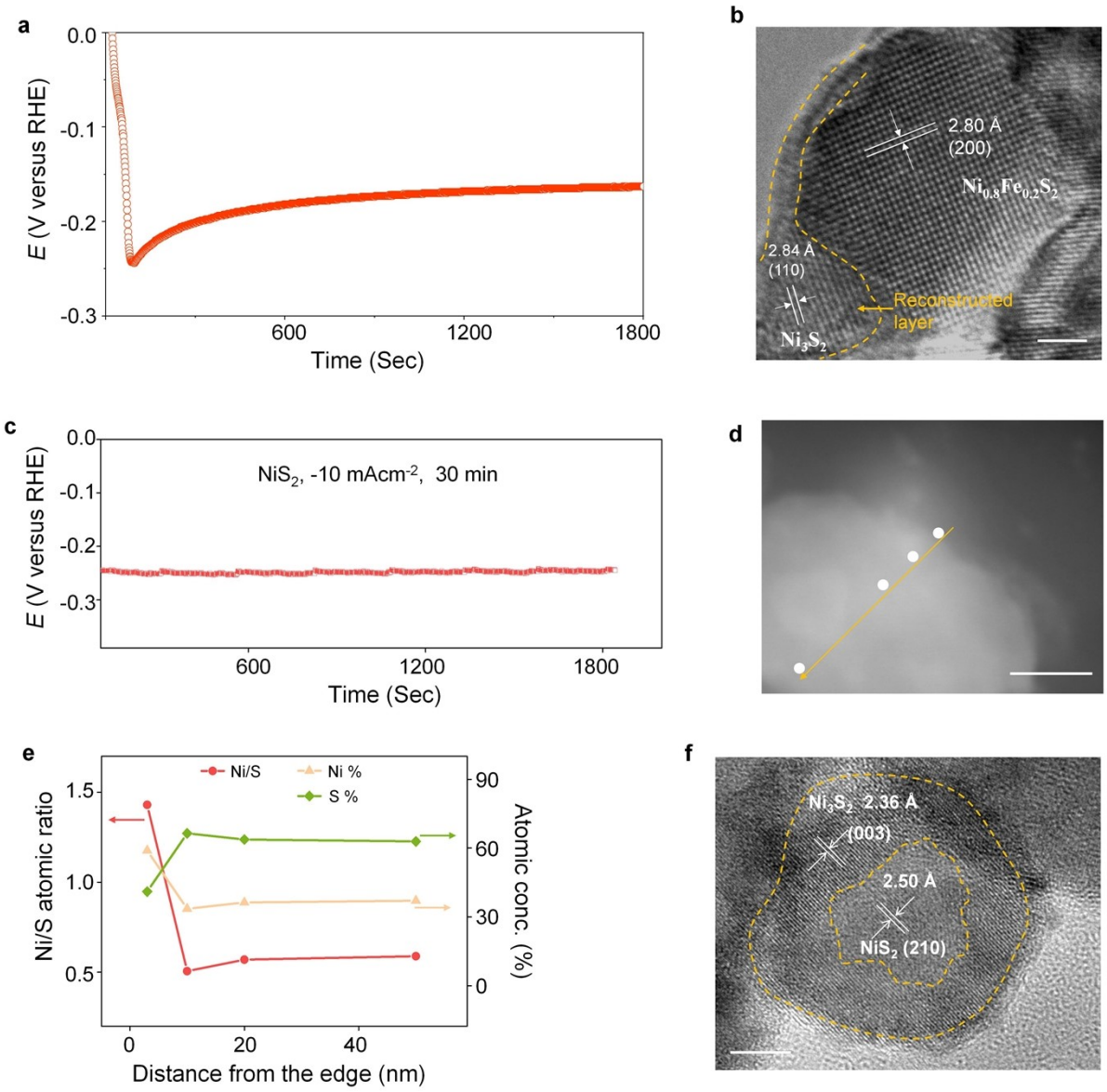

Figure S13. TEM characterization of surface-restructured nickel sulfide after the process of HER. The post-reaction catalysts attached to carbon fiber paper are obtained by using a sonicator. **a**, Chronopotentiometric curves obtained with $Ni_{0.8}Fe_{0.2}S_2$ at constant current density of 10 mA cm^{-2}. **b**, HRTEM image of post-electrolysis $Ni_{0.8}Fe_{0.2}S_2$. Scale bar, 2 nm. **c**, Chronopotentiometric curves obtained with NiS_2 at constant current density of 10 mA cm^{-2}. **d**, **e**, Elemental composition of post-electrolysis NiS_2 determined from EDS at a series of spots along a line from the crystallite edge to the bulk reveals the variation in Ni:S composition across the crystallite, the marked points in (**d**) denote the scanning distance along the pathway in nm. **f**, HRTEM image of post-electrolysis NiS_2. The scale bars are 20 nm in (**d**), 5 nm in (**f**).

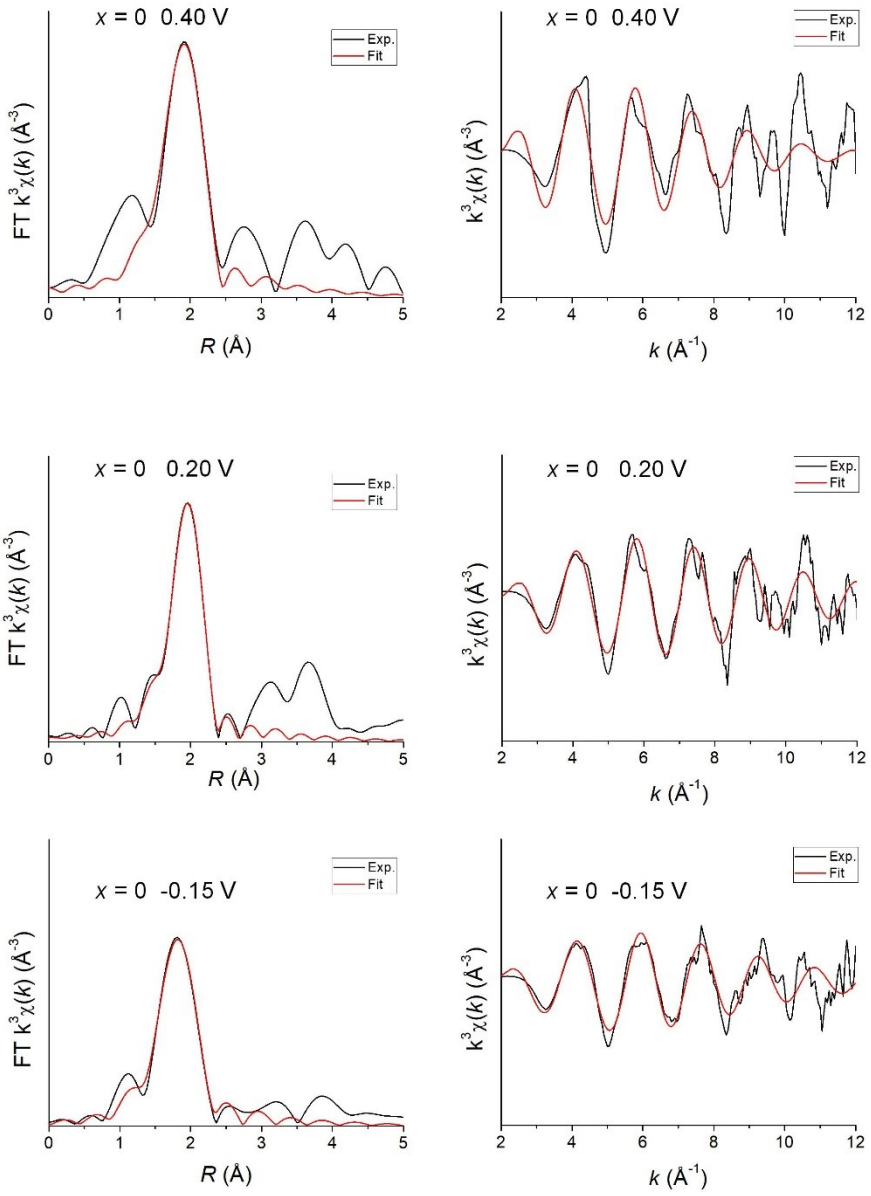

Figure S14. Ni K-edge EXAFS analysis of nickel sulfide in *R* and *k* spaces. FT-EXAFS spectra and fits of Ni K-edges from NiS_2 (in -0.15 V, 0.20 V and 0.40 V vs. RHE). The black lines represent the experiment data and the red lines represent the fitting values.

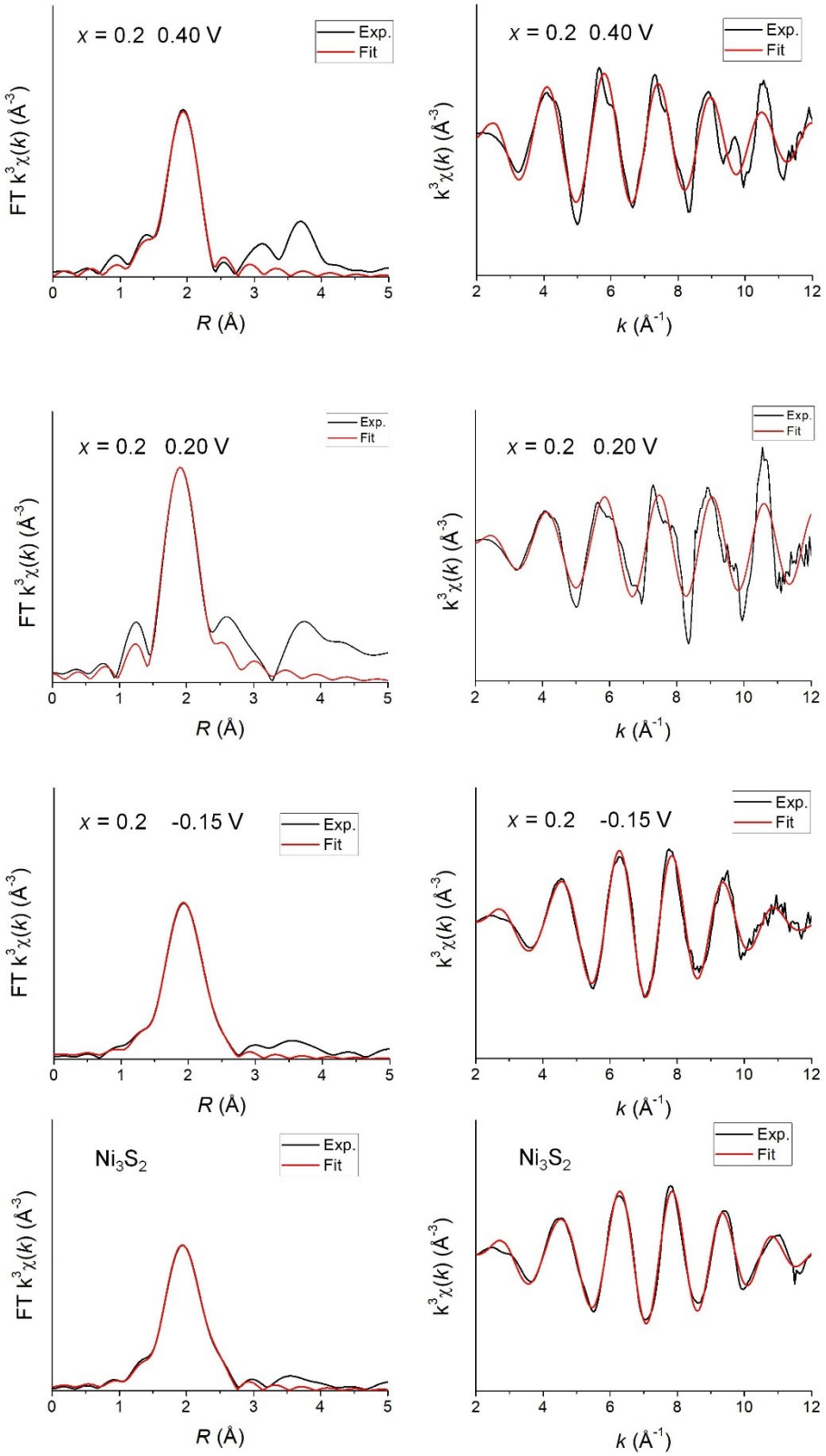

Figure S15. Ni K-edge EXAFS analysis of nickel sulfide in *R* and *k* spaces. FT-EXAFS spectra and fits of Ni K-edges from Ni_3S_2 catalysts and $Ni_{0.8}Fe_{0.2}S_2$ (in -0.15 V, 0.20 V and 0.40 V vs. RHE). The black lines represent the experiment data and the red lines represent the fitting values.

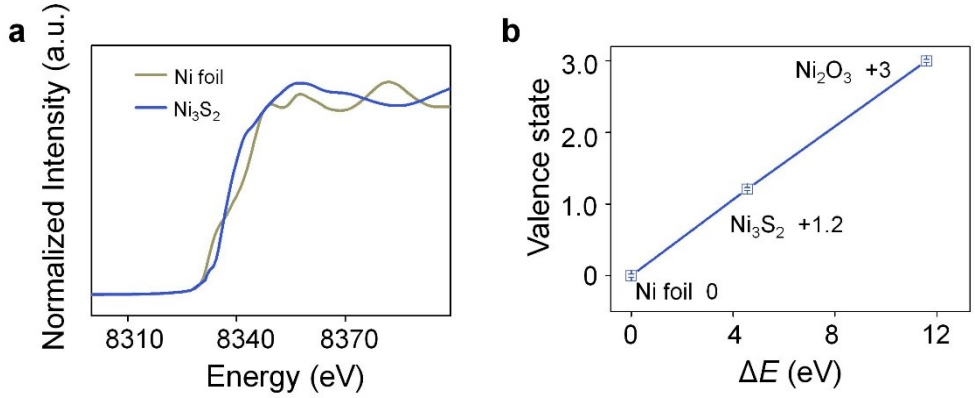

Figure S16. XAFS measurements. **a**, **b** is the Ni_3S_2 XANES spectra and the corresponding valence state of Ni in Ni_3S_2 according to the linear relationship described in (**b**). Error bars represent the standard deviation from at least three independent measurements. The average valence state of nickel foil and Ni_2O_3 is fitted to 0 and +3 by the Nickel K-edge XANES in Figure S4. Applying the linear correlation, it was found that the average valence state of Ni for Ni_3S_2 is approximately +1.20.

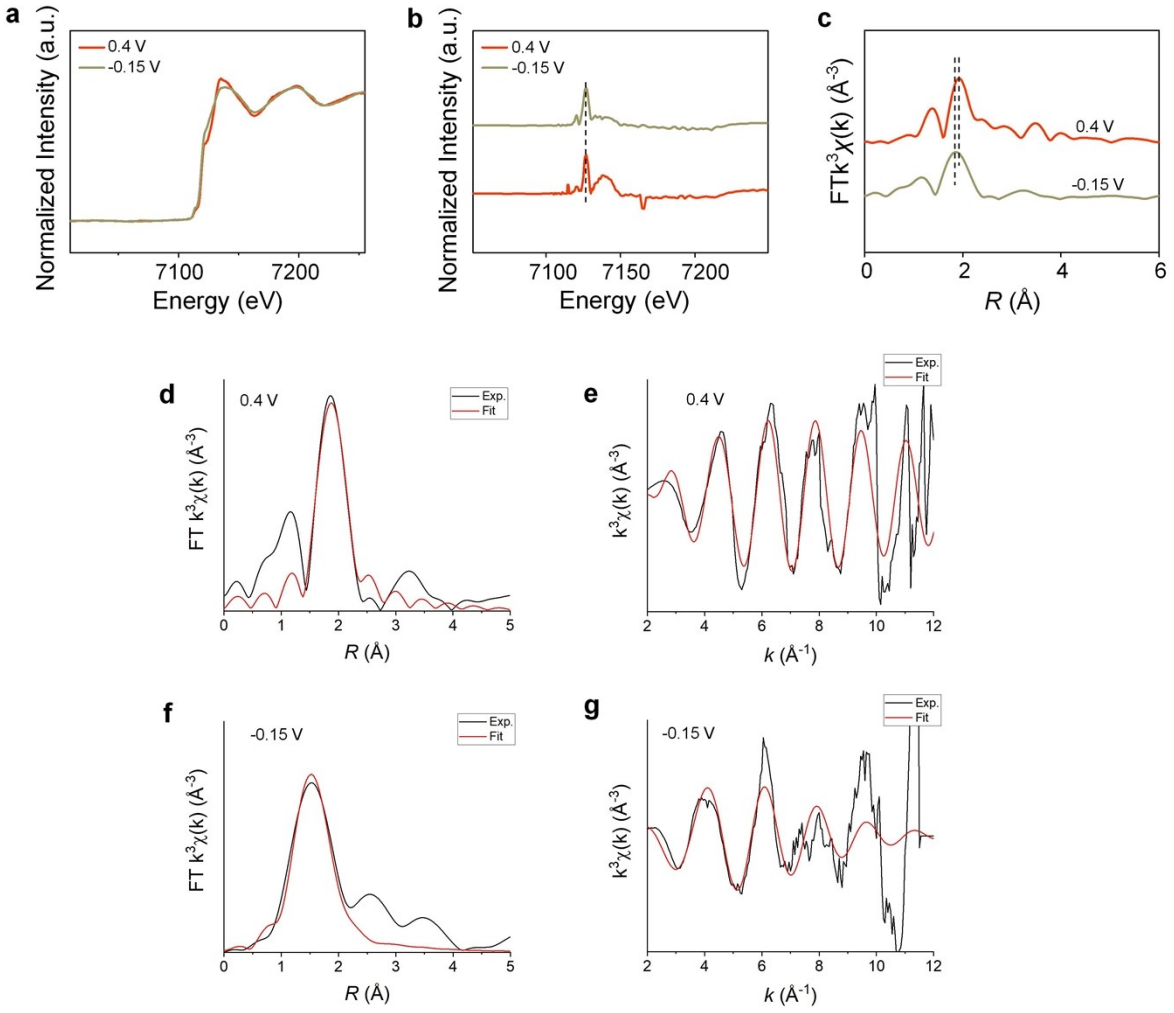

Figure S17. Operando XAFS spectra characterization of $Ni_{0.8}Fe_{0.2}S_2$ catalysts. **a**, Normalized operando Fe K-edge XANES analysis at 0.40 and -0.15 V (vs. RHE). **b**, Normalized difference spectra for Fe K-edge XANES. **c**, the corresponding operando FT k^3-weighted EXAFS. **d** ~ **g**, FT-EXAFS spectra and fits of Fe K-edges in *R* and *k* spaces. The black lines represent the experiment data and the red lines represent the fitting values.

Absorption Fe K-edges of $Ni_{0.8}Fe_{0.2}S_2$ present insignificant shift with the potential increase cathodically, clearly explaining the valence state of Fe keep stable at 2+ during HER process. Compared with the profiles collected at 0.4 V vs. RHE from the FT-EXAFS spectra in *R*-space, the Fe-S bond peak decrease at -0.15 V vs. RHE, indicating Fe atom accumulating in Fe-S_4 tetrahedral coordination resulted from reconstruction. For fitting results (Figure S17 d~g), the Fe-S CN decreases from 4.6±1.1 to 3.3±1.9 for $Ni_{0.8}Fe_{0.2}S_2$ at 0.20 and -0.15 V (Table S3). Similarly, the Fe-S bond (2.2 Å±0.03) of $Ni_{0.8}Fe_{0.2}S_2$ at -0.15 V is decreased from 2.3 Å±0.03.

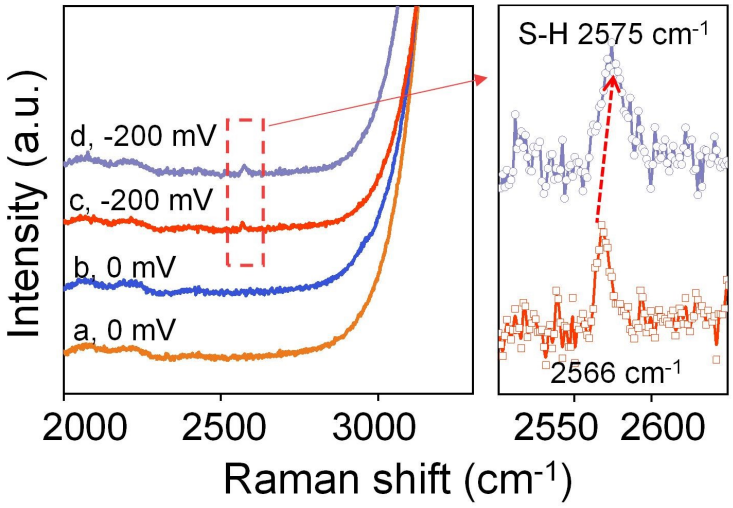

Figure S18. In-situ Raman spectra of catalysts at the overpotential of 0 mV and −200 mV from 2000 to 3300 cm^{-1}. a, NiS_2 at 0 mV. b, $Ni_{0.8}Fe_{0.2}S_2$ at 0 mV. c, NiS_2 at -200 mV. d, $Ni_{0.8}Fe_{0.2}S_2$ at -200 mV.

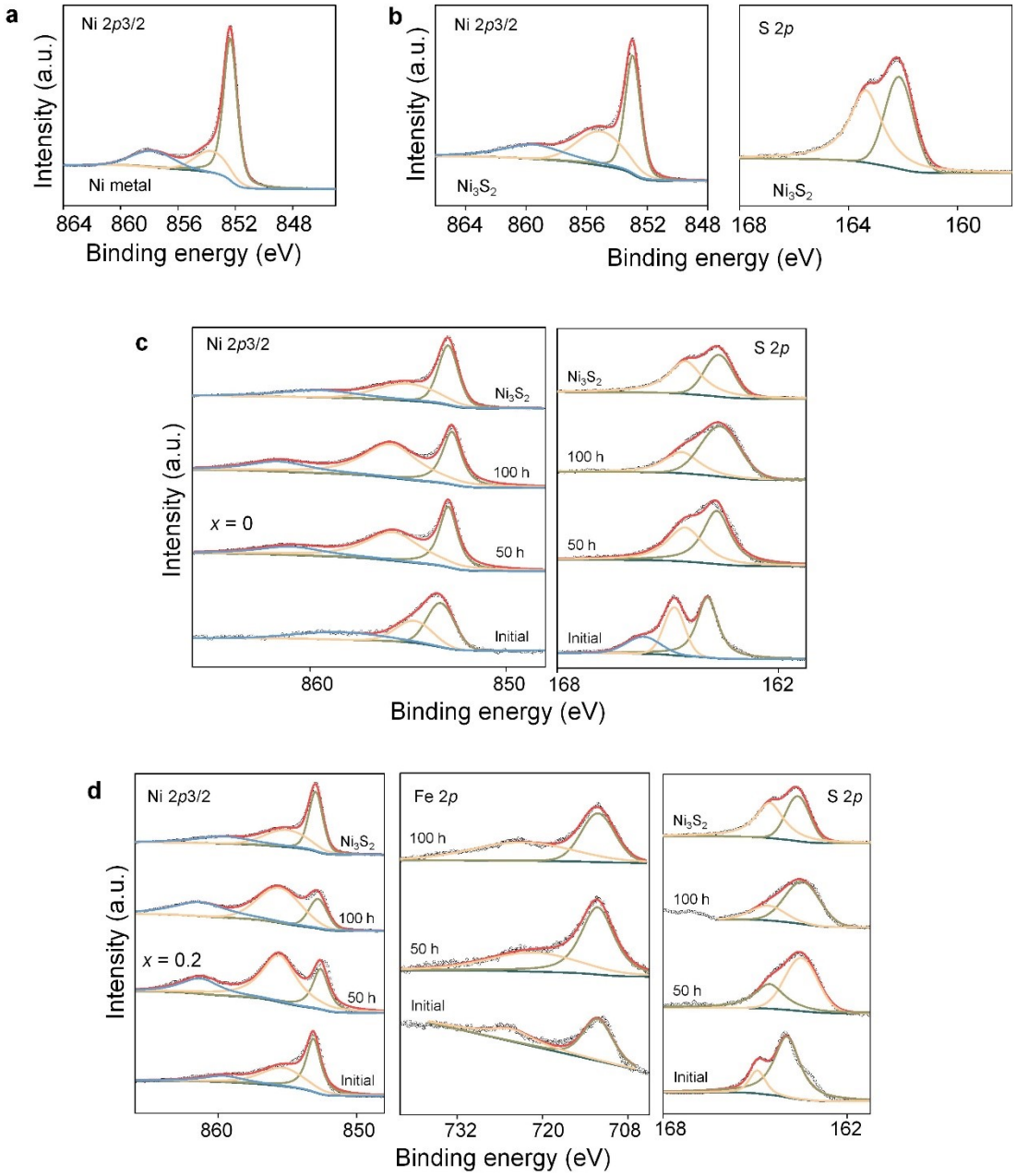

Figure S19. XPS Characterization. **a**, Ni 2*p*3/2 region of Ni Metal. **b**, Ni 2*p*3/2 and S 2*p* regions of Ni_3S_2. The Ni metal peak is at 852.30 eV, and the Ni peak of Ni_3S_2 is about at 852.85 eV. **c**, **d**, XPS analysis of catalysts after long-term operation to identify the binding energy and ratio of the surface element for NiS_2 (**c**) and $Ni_{0.8}Fe_{0.2}S_2$ (**d**). At 50 h and 100 h, the Ni 2*p*3/2 binding energy is approaching to Ni in Ni_3S_2, while for Fe, the binding energy is slightly changed.

For the Ni 2*p*2/3, the peaks after 50 h and 100 h were all verge on the corresponding peaks of the Ni_3S_2 crystal, implying the finalized phase of the long-term service also close to Ni_3S_2 structure.

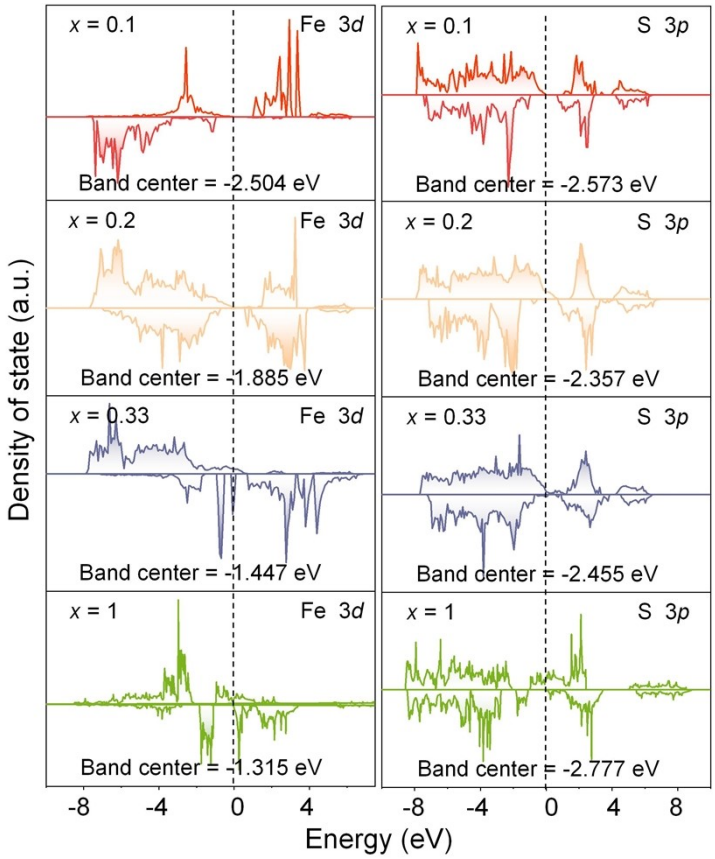

Figure S20. Computed Fe 3*d*, S 3*p* PDOS of $Ni_{1-x}Fe_xS_2$ (x = 0.1, 0.2, 0.33, 1). x = 1 stand for FeS_2 catalysts.

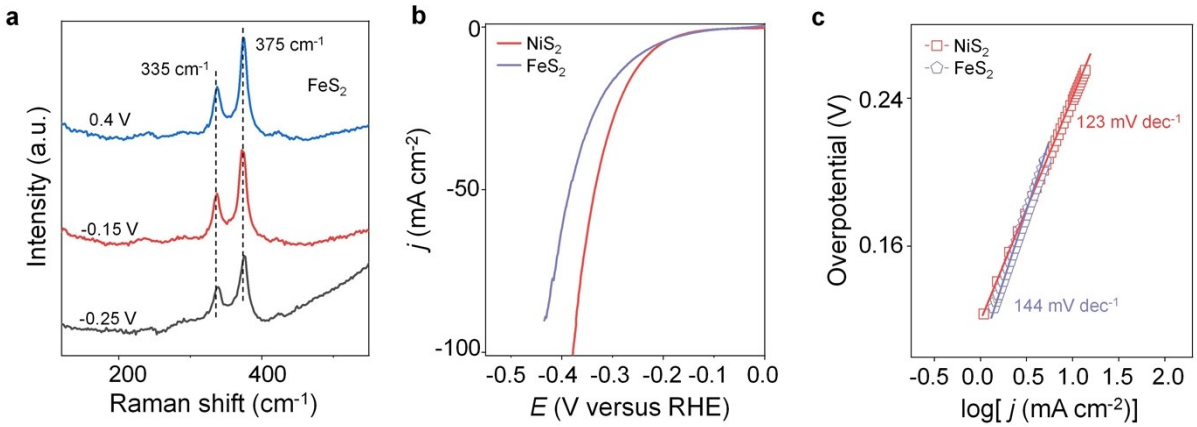

Figure S21. a, In-situ Raman spectra of FeS_2 (at 335cm^{-1} and 375cm^{-1}) samples at the potentials of 0.4~-0.25 V (vs. RHE) in 1M KOH. **b**, HER polarization curves of NiS_2 and FeS_2 catalysts on carbon fiber paper in N_2-saturated 1M KOH, **c**, Corresponding HER Tafel plots derived from the polarization curves.

As displayed in Figure S2, the diffraction peaks by XRD of as-prepared $Ni_{1-x}Fe_xS_2$ ($x \approx 0$~0.33) appeared the segregation of FeS_2, when $x \geq 0.25$. In order to evaluate the phase evolution process and the performance of HER for FeS_2, we prepared FeS_2 catalysts based on the preparation methods of NiS_2 catalysts in the manuscript. Figure S21a presented that the as-prepared FeS_2 catalysts remained the structure stable at -0.25 V vs. RHE and did not undergo the phase transition process during the HER process. Further analysis of the polarization curve and the Tafel slope in Figure S21 b, c, it showed that the HER activity was inferior for FeS_2 catalysts for comparing with NiS_2.

The formation of inferior FeS_2 might impact the phase transition process of nickel sulfides to generate different active species. Indeed, the declined ECSA for nickel sulfides of x = 0.25 and 0.33 ($Ni_{0.8}Fe_{0.2}S_2$, 53.28 mF cm^{-2}; $Ni_{0.75}Fe_{0.25}S_2$, 43.59 mF cm^{-2} and $Ni_{0.67}Fe_{0.33}S_2$, 34.7 mF cm^{-2}) established this. Therefore, when the Fe doping content was greater than 20%, the electrochemical activity of HER was declined.

Moreover, excessive Fe substitution ($x \geq 0.25$) in $Ni_{1-x}Fe_xS_2$ could make a small part of FeS_2 segregation, and the remaining Fe existed in the active structure (Ni_3S_2) after the phase transition process, which could also induce a great effect on the HER performance (discussed in Figure S22).

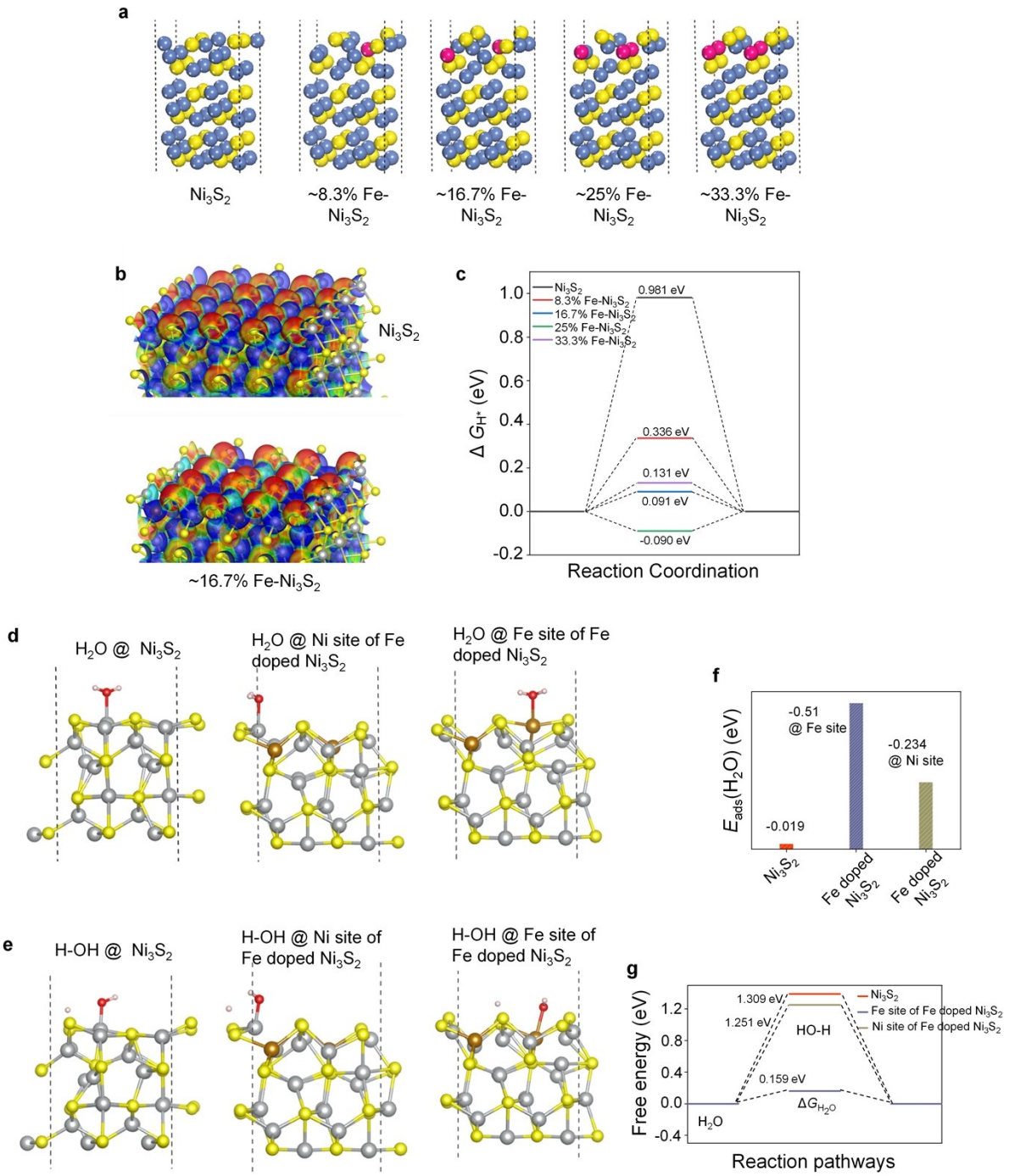

Figure S22. a, The illustrations of Ni_3S_2 (101) and the Fe-doped Ni_3S_2 structure with different doping concentration for calculation. **b**, Electrondensity isosurface of ideal Ni_3S_2 (101) and 16.7% Fe doped Ni_3S_2 (101). The electron-density isosurfaces are plotted at 0.02 *e* $bohr^{-3}$. Red color means lower electrostatic potential, blue color means higher electrostatic potential. **c**, Calculated free-energy diagram of HER. **d**, **e**, Water adsorption and dissociation pathways and relevant structures on different substrates. **f**, The calculated adsorption free energy changes of H_2O on Ni_3S_2 and 16.7% Fe doped Ni_3S_2. **g**, The Gibbs free energy change for formation of H-OH intermediates (ΔG_{H2O}, water dissociation step) of catalysts.

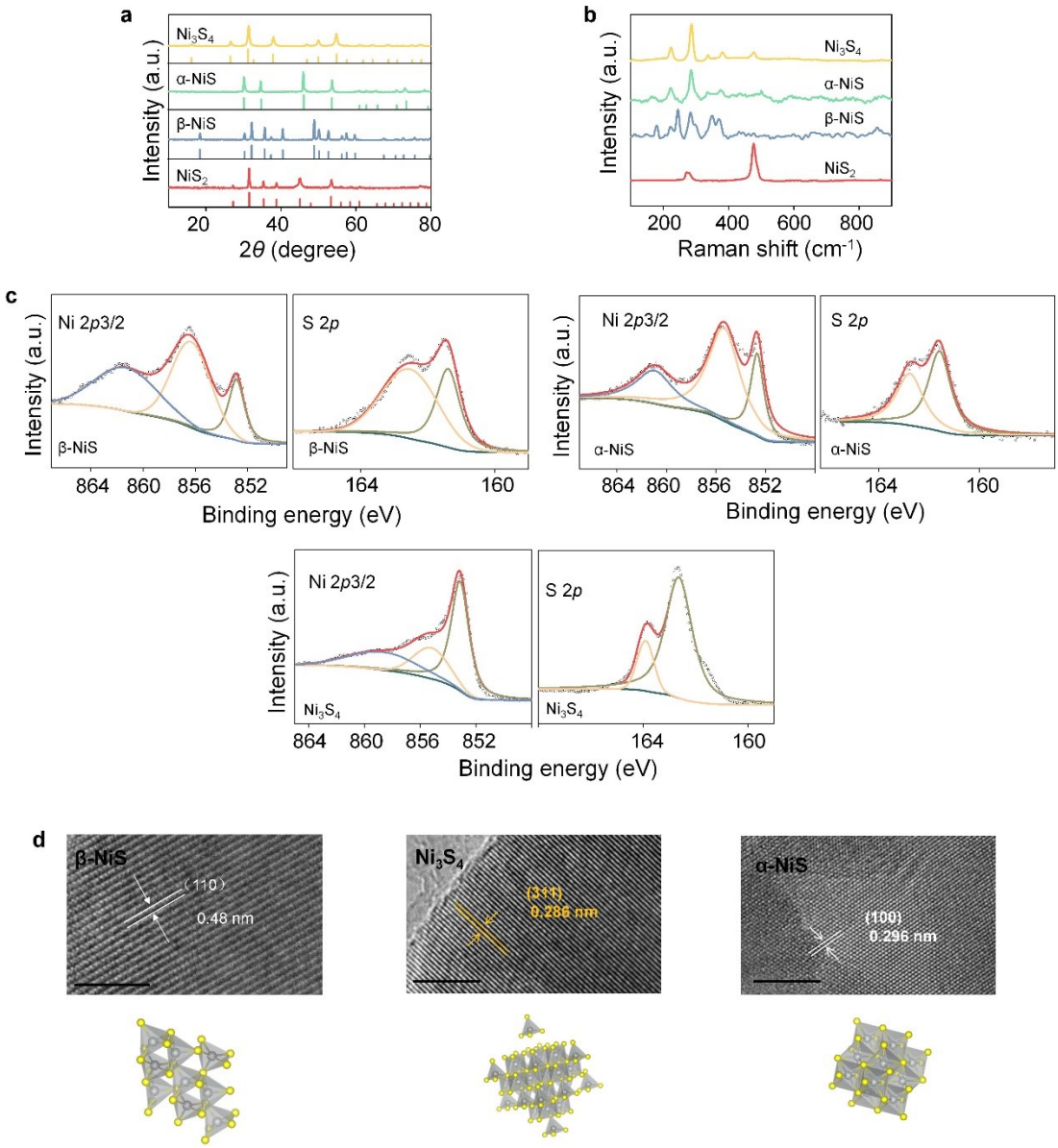

Figure S23. Structure Characterization of α-NiS, β-NiS Ni_3S_4. **a,** PXRD. **b**, Raman spectra. The Raman peaks were shown in Supplementary Table 4. **c**, XPS analysis of the electrodes of α-NiS, β-NiS and Ni_3S_4. **d**, HRTEM characterization of α-NiS, β-NiS and Ni_3S_4 and the lattice structure of each nickel sulfides. Scale bars, 5 nm. For spinel structure of Ni_3S_4, there was two arrangement of Ni atom and S atom to consist octahedron polyhedral of Ni with six S around and tetrahedron polyhedral of Ni with four S. For β-NiS, there was five S around Ni atom to consist pyramidal polyhedral. For the α-NiS, the Ni atom was around with six S atom to consist octahedron polyhedral.

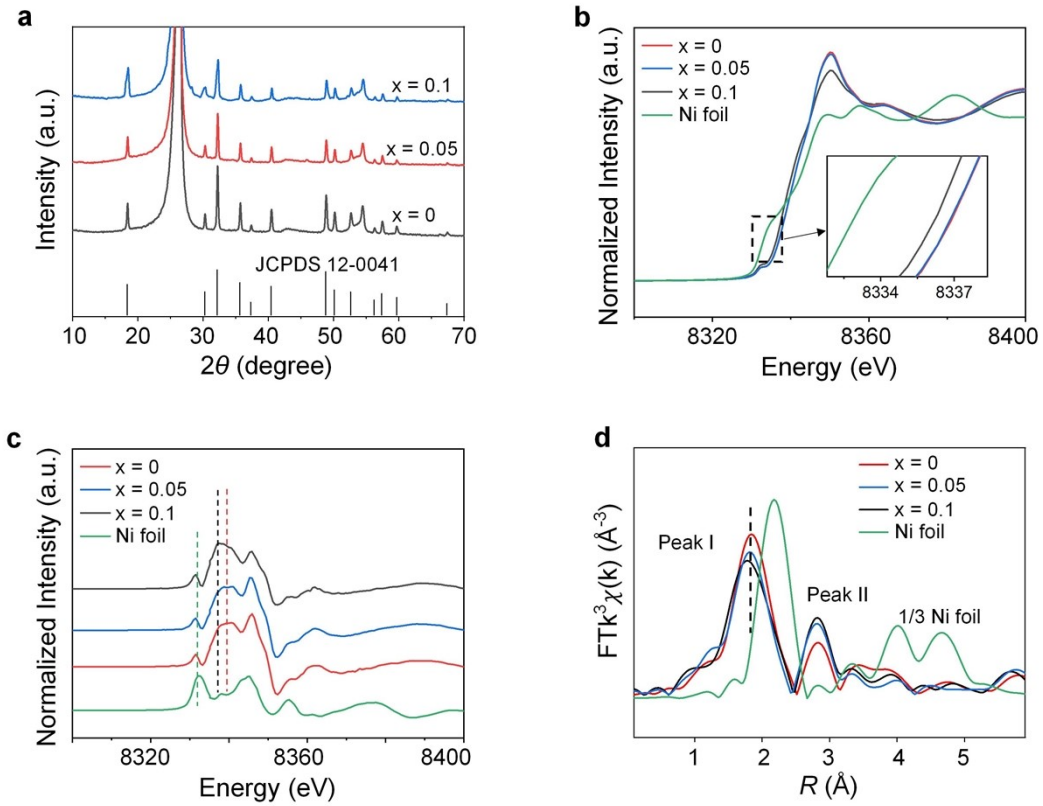

Figure S24. Structural characterizations of as-prepared β-$Ni_{1-x}Fe_xS$ catalysts. **a**, XRD patterns of synthesized β-$Ni_{1-x}Fe_xS$ ($x \approx 0$~0.1) samples. **b**, Normalized Ni K-edge XANES analysis of β-$Ni_{1-x}Fe_xS$ samples with Ni foil as reference. Inset, Magnified pre-edge XANES region. **c**, Normalized difference spectra for Ni K-edge XANES. **d**, The corresponding k^3-weighted Fourier transform (FT) Ni K-edge EXAFS spectra. Peaks I and II in the FT-EXAFS plots are assigned to Ni-S and Ni-Ni bonds, respectively.

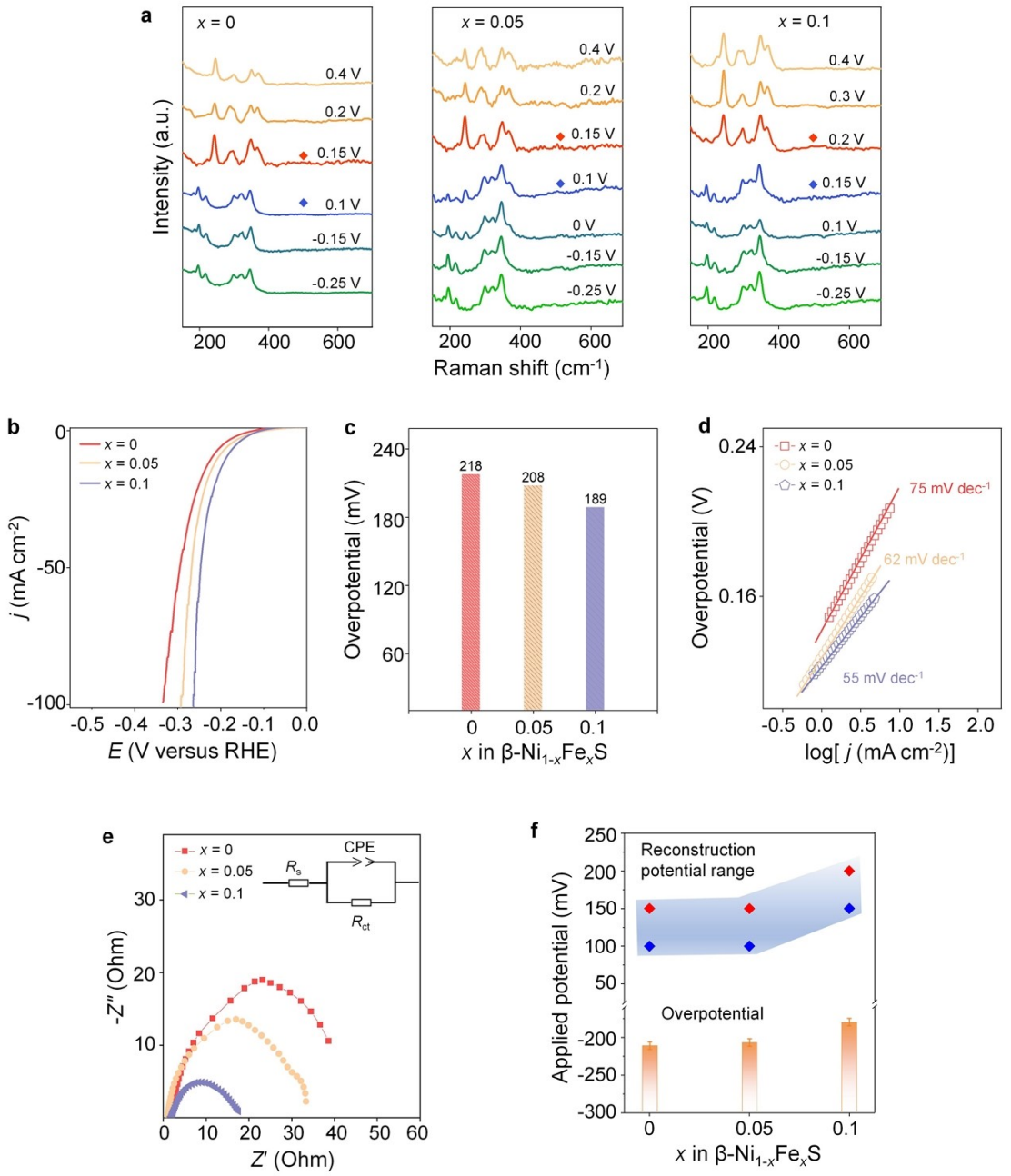

Figure S25. a, In-situ Raman spectra of β-$Ni_{1-x}Fe_xS$ (x = 0, 0.05, 0.1) samples. The red diamond dots represent the final potential of existence for Raman peaks of β-$Ni_{1-x}Fe_xS$ structures, and the blue diamond dots stand for the potential of emerging of Ni_3S_2 Raman peaks. **b**, HER polarization curves of β-$Ni_{1-x}Fe_xS$ catalysts. **c**, Overpotential of the nickel sulfide catalysts at the current density of 10 $mAcm^{-2}$. **d**, Corresponding HER Tafel plots derived from the polarization curves. **e**, Nyquist plots of the catalyst electrode @200 mV overpotential. Inset of (**e**) is the simplified Randles equivalent circuit model. **f**, The surface reconstruction potential threshold range for β-$Ni_{1-x}Fe_xS$ (x = 0, 0.05, 0.1) samples, and the corresponding overpotentials (@10 $mAcm^{-2}$) are plotted to show the dynamic correlation of structure-activity.

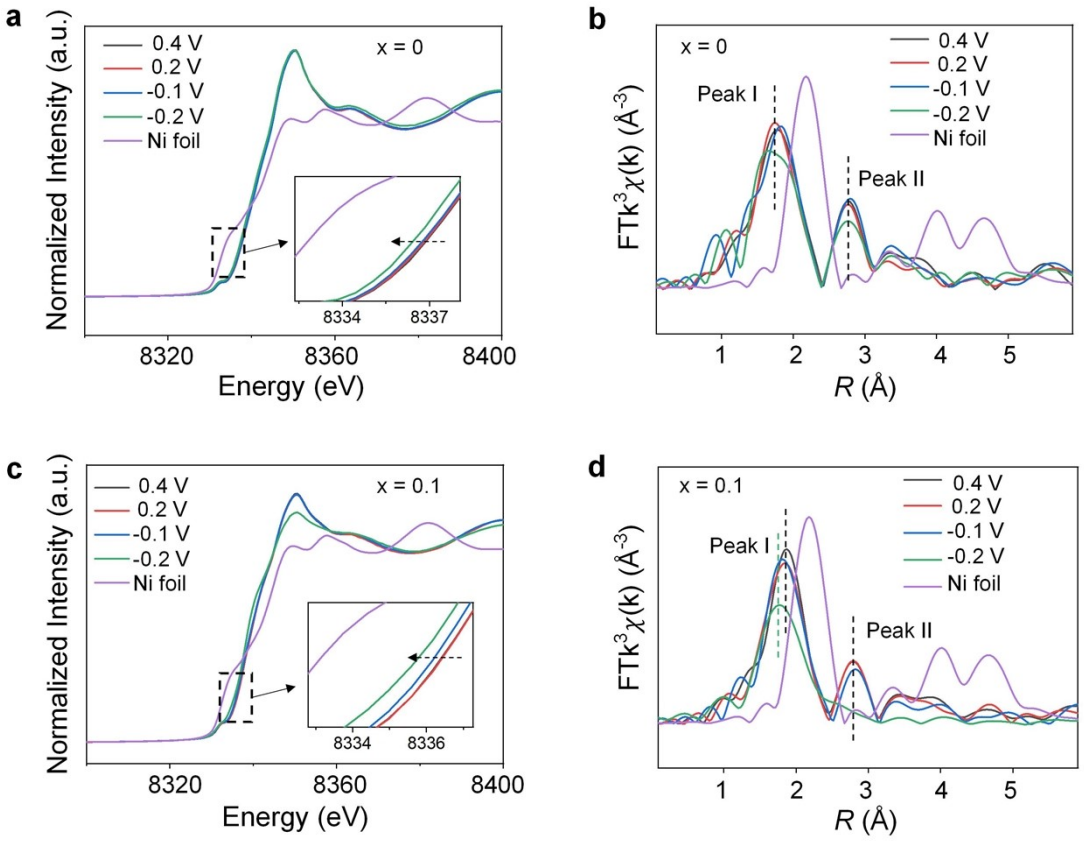

Figure S26. Operando XAFS characterization of catalysts. **a**, Normalized operando Ni K-edge XANES analysis of β-NiS (x = 0) at 0.40, 0.20, -0.1 and -0.2 V (vs. RHE) with Ni Foil as reference. Inset, Magnified pre-edge XANES region. **b**, The corresponding operando FT k^3-weighted Ni K-edge EXAFS of β-NiS (x = 0). **c**, Normalized operando Ni K-edge XANES analysis of β-$Ni_{0.9}Fe_{0.1}S$ (x = 0.1) at 0.40, 0.20, -0.1 and -0.2 V (vs. RHE) with Ni Foil as reference. Inset, Magnified pre-edge XANES region. **d**, The corresponding operando FT k^3-weighted Ni K-edge EXAFS of β-$Ni_{0.9}Fe_{0.1}S$ (x = 0.1).

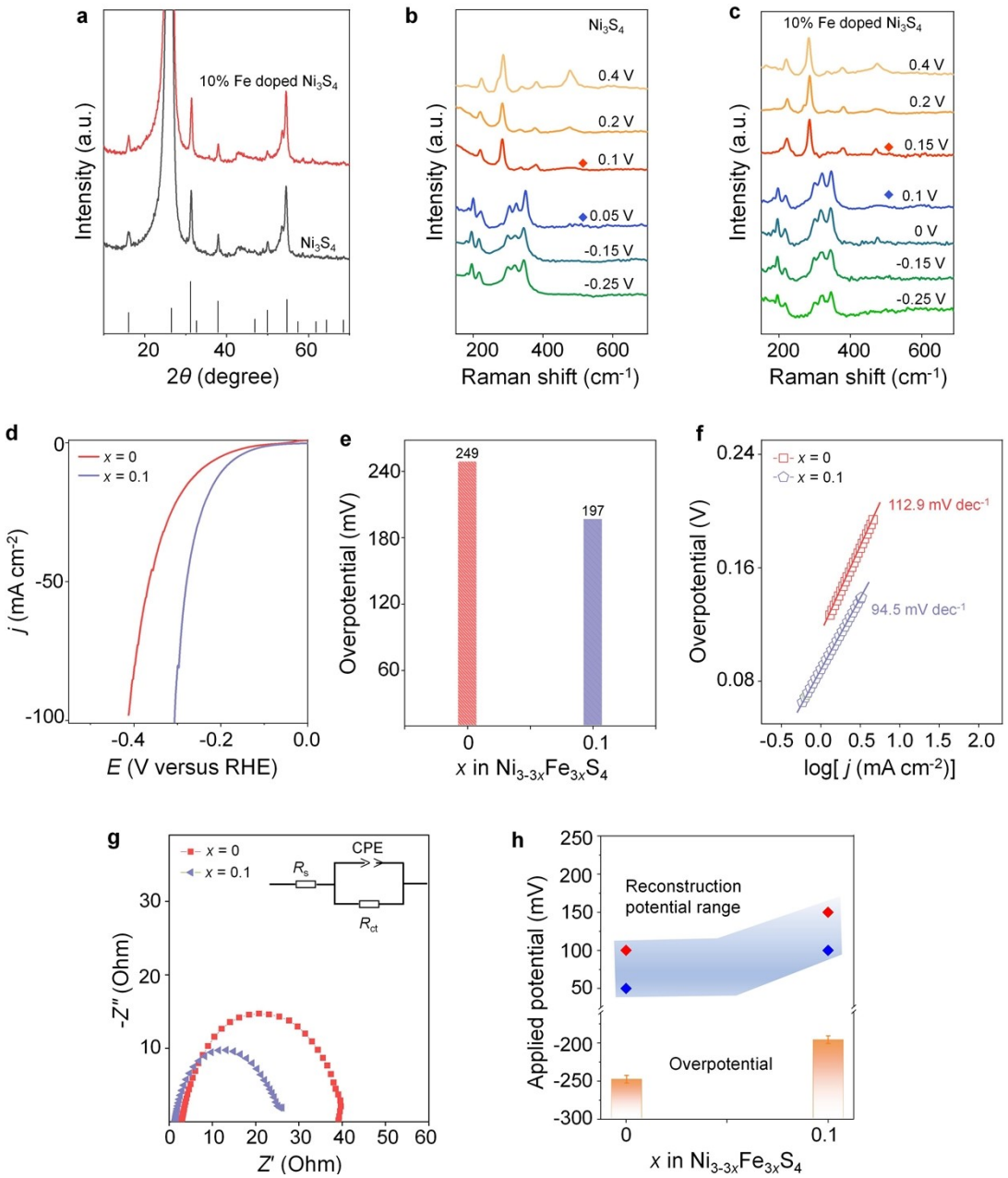

Figure S27. a, XRD patterns of synthesized $Ni_{3-3x}Fe_{3x}S_4$ (x = 0, 0.1) samples. **b**, **c**, In-situ Raman spectra of $Ni_{3-3x}Fe_{3x}S_4$ (x = 0, 0.1). The red diamond dots represent the final potential of existence for Raman peaks of $Ni_{3-3x}Fe_{3x}S_4$ structures, and the blue diamond dots stand for the potential of emerging of Ni_3S_2 Raman peaks. **d**, HER polarization curves of $Ni_{3-3x}Fe_{3x}S_4$ catalysts. **e**, Overpotential of the nickel sulfide catalysts at the current density of 10 $mAcm^{-2}$. **f**, Corresponding HER Tafel plots. **g**, Nyquist plots of the catalyst electrode @200 mV overpotential. Inset of (**g**) is the simplified Randles equivalent circuit model. **h**, the surface reconstruction potential threshold range for $Ni_{3-3x}Fe_{3x}S_4$ (x = 0, 0.1) samples, and the corresponding overpotentials (@10 $mAcm^{-2}$) are plotted to show the dynamic correlation of structure-activity.

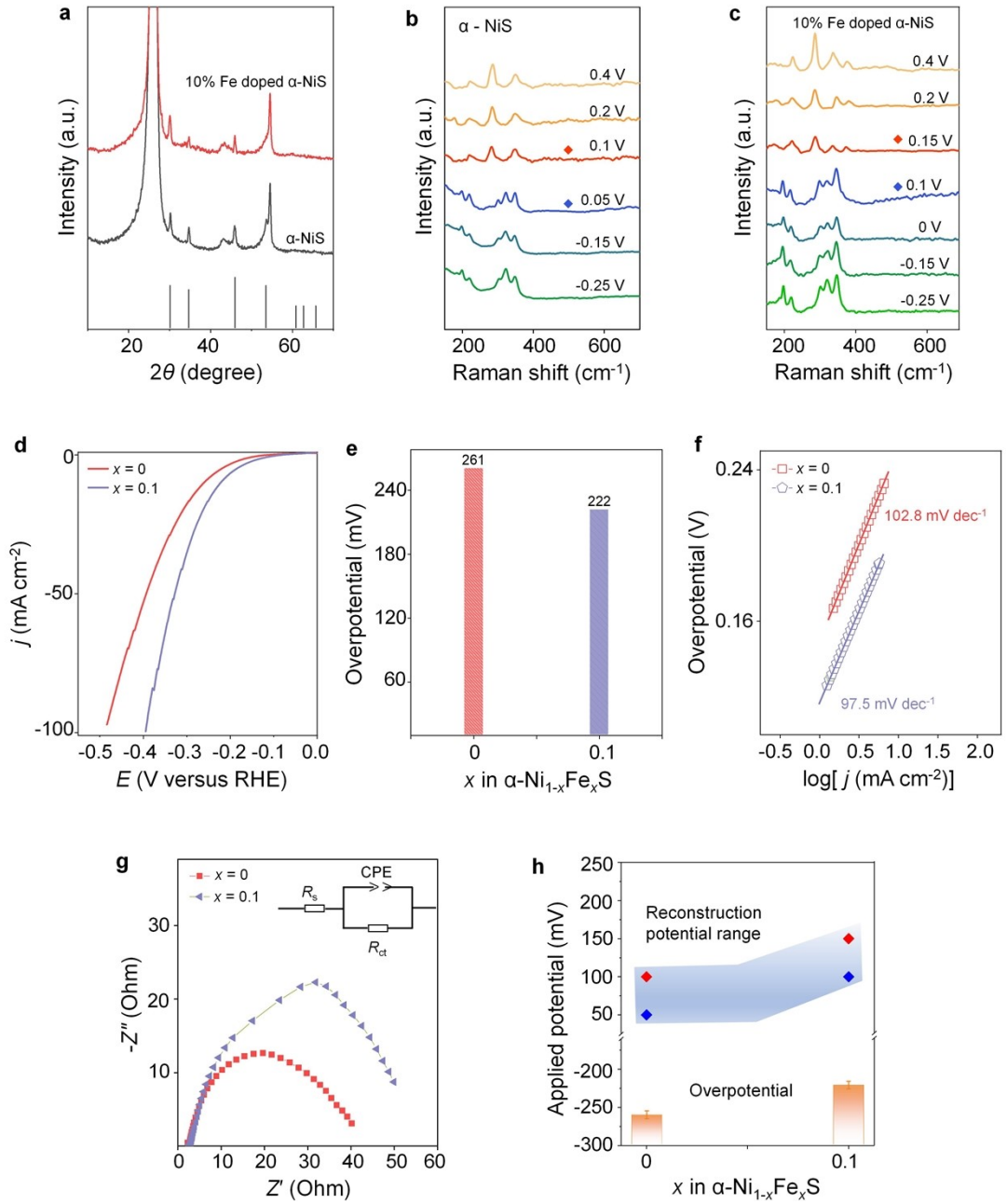

Figure S28. a, XRD patterns of synthesized α-$Ni_{1-x}Fe_xS$ (x = 0, 0.1). **b**, **c**, In-situ Raman spectra of α-$Ni_{1-x}Fe_xS$ (x = 0, 0.1) samples. The red diamond dots represent the final potential of existence for Raman peaks of α-$Ni_{1-x}Fe_xS$ structures, and the blue diamond dots stand for the potential of emerging of Ni_3S_2 Raman peaks. **d**, HER polarization curves of α-$Ni_{1-x}Fe_xS$ catalysts. **e**, Overpotentials at the current density of 10 $mAcm^{-2}$. **f**, Corresponding HER Tafel plots derived from the polarization curves. **g**, Nyquist plots of the catalyst electrode @200 mV overpotential. Inset of (**g**) is the simplified Randles equivalent circuit model. **h**, the surface reconstruction potential threshold range for α-$Ni_{1-x}Fe_xS$ (x = 0, 0.1) samples, and the corresponding overpotentials (@10 $mAcm^{-2}$) are plotted to show the dynamic correlation of structure-activity.

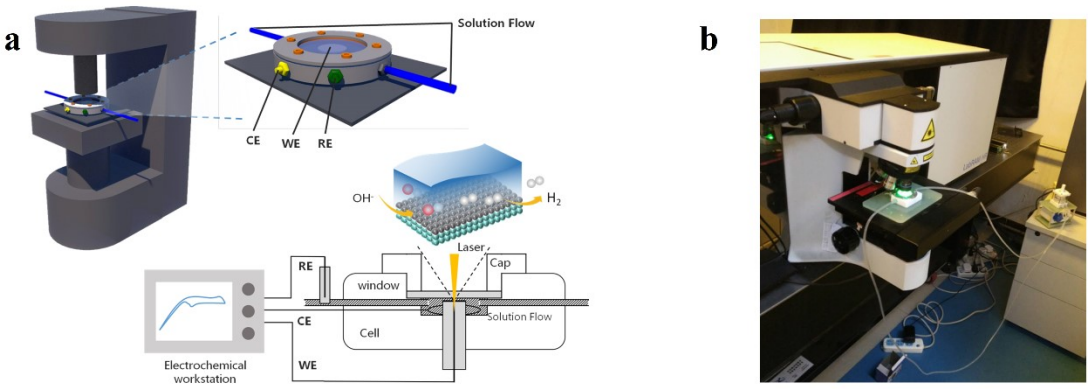

Figure S29. Equipment used for in-situ Raman measurements. **a**, Schematic for the equipment used for in-situ Raman. **b**, Digital photo taken during in-situ Raman.

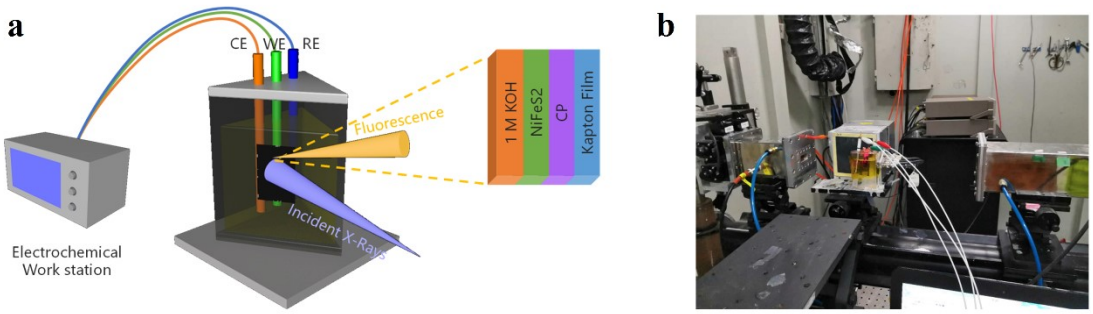

Figure S30. Equipment used for operando XAFS measurements. **a**, Schematic for the equipment used for operando XAFS measurements. **b**, Digital photo taken during operando XAFS measurement.

Supporting Tables

Table S1. The Ni and Fe K-edge positions, nominal Ni and Fe valence state and the nominal sulphur vacancy concentration (δ) in $Ni_{1-x}Fe_xS_{2-\delta}$.

Samples	Fe k-edge		Samples	Ni k-edge		Nominal sulphur vacancy concentration (δ)
	Edge energy (eV)	Nominal Valence state		Edge energy (eV)	Nominal Valence state	
Fe foil	7112.00	0.00	Ni foil	8333.00	0.00	
Fe_2O_3	7122.32	3.00	Ni_2O_3	8344.61	3.00	
			$x = 0$	8340.68	1.98	$\delta = 0.02$ ($NiS_{1.98}$)
$x = 0.1$	7118.92	2.01	$x = 0.1$	8340.35	1.90	$\delta = 0.09$ ($Ni_{0.9}Fe_{0.1}S_{1.91}$)
$x = 0.2$	7118.98	2.03	$x = 0.2$	8340.12	1.84	$\delta = 0.13$ ($Ni_{0.8}Fe_{0.2}S_{1.87}$)
$x = 0.33$	7118.89	2.00	$x = 0.33$	8340.27	1.88	$\delta = 0.08$ ($Ni_{0.67}Fe_{0.33}S_{1.92}$)

The nominal sulphur vacancy concentration was calculated on the basis of the nominal valence state of Ni, Fe and S.

Table S2. XPS fitting parameters of binding energies for the as-prepared nickel sulfide catalysts.

Catalyst	Binding energy (eV)					Element Ratio (%) Ni : (Fe): S
	Ni 2*p*3/2	S 2*p*3/2	S 2*p*1/2	Fe 2*p*3/2	Fe 2*p*1/2	
Ni Metal	852.30	—	—	—	—	—
Ni_3S_2	852.82	162.18	163.36	—	—	23.85:27.57
NiS_2	853.56	162.58	163.79	—	—	4.01:10.26
$Ni_{0.9}Fe_{0.1}S_2$	853.13	162.7	163.8	710.87	726.92	8.69: (1.03): 20.24
$Ni_{0.8}Fe_{0.2}S_2$	853.16	162.63	163.92	710.65	722.85	10.52: (1.47) : 21.05
NiS_2, 50 h	852.89	162.26	163.43	—	—	26.03:16.33
NiS_2, 100 h	852.68	162.25	163.80	—	—	22.92:13.28
$Ni_{0.8}Fe_{0.2}S_2$, 50 h	852.59/ 855.56	162.25	163.48	711.05	722.08	20.09: (1.16): 10.27
$Ni_{0.8}Fe_{0.2}S_2$, 100 h	852.77/ 855.50	162.10	163.47	711.12	722.28	21.02: (0.95) : 16.20
α-NiS	852.71/ 855.38	161.59	162.79	—	—	16.42:10.84
β-NiS	852.89/ 856.52	161.41	162.60	—	—	10.36:14.93
Ni_3S_4	853.17/ 855.32	162.68	163.90	—	—	13.32:35.22

Table S3. EXAFS fitting parameters at the Ni K-edge and Fe K-edge of various samples（S_0^2 = 0.82）

Sample	Path	CN[a]	R (Å)[b]	$\sigma^2\times10^{-3}$ (Å^2)[c]	ΔE (eV)[d]	R factor
Ni foil	Ni-Ni	12*	2.48 ± 0.01	6.1 ± 0.2	6.7 ± 0.3	0.001
x = 0	Ni-S	6.0 ± 0.7	2.40 ± 0.01	7.4 ± 1.8	2.0 ± 1.9	0.015
x = 0.1	Ni-S	5.9 ± 0.6	2.39 ± 0.01	8.2 ± 1.5	3.5 ± 1.5	0.010
x = 0.2	Ni-S	5.8 ± 0.6	2.38 ± 0.01	8.2 ± 2.1	1.4 ± 1.8	0.007
x = 0.33	Ni-S	5.4 ± 0.6	2.36 ± 0.02	10.9 ± 3.2	1.6 ± 2.7	0.016
Ni_3S_2	Ni-S	3.9 ± 0.4	2.27 ± 0.02	6.8 ± 2.4	3.8 ± 1.6	0.001
	Ni-Ni	2.0 ± 1.1	2.52 ± 0.03	6.2 ± 4.0	4.6 ± 4.6	
x = 0.2 0.40 V	Ni-S	5.9 ± 0.6	2.38 ± 0.01	7.3 ± 0.9	1.3 ± 1.1	0.008
x = 0.2 0.20 V	Ni-S	4.1 ± 0.4	2.36 ± 0.01	2.5 ± 1.6	0.9 ± 2.2	0.011
x = 0.2 -0.15 V	Ni-S	3.5 ± 0.4	2.26 ± 0.02	6.2 ± 2.5	2.4 ± 2.2	0.001
	Ni-Ni	2.8 ± 1.6	2.51 ± 0.03	7.7 ± 4.5	0.1 ± 5.9	
x = 0 0.40 V	Ni-S	6.0 ± 0.7	2.39 ± 0.01	4.6 ± 1.3	1.5 ± 1.8	0.018
x = 0 0.20 V	Ni-S	6.0 ± 0.6	2.38 ± 0.01	6.1 ± 1.4	1.4 ± 1.1	0.016
x = 0 -0.15 V	Ni-S	4.9 ± 0.5	2.30 ± 0.01	8.7 ± 1.7	-3.7 ± 1.9	0.013
x = 0.2 0.40 V	Fe-S	4.6±1.1	2.30±0.02	2.6±2.2	5.9±2.7	0.015
x = 0.2 -0.15 V	Fe-S	3.3±1.9	2.20±0.03	12.3±5.8	-6.4±4.8	0.019

[a]CN: coordination number; [b]R: bond distance; [c]σ^2: Debye-Waller factors; [d]ΔE: the inner potential correction. R factor: goodness of fit. * The experimental EXAFS fit of metal foil by fixing CN as the known crystallographic value.

Table S4. Raman spectra of different nickel sulfides.

	Raman Peaks (cm^{-1})								
NiS_2	274.4	284.8	479.3						
Ni_3S_2	187.6	202.1	223.6	303.6	324.6	350.3			
Ni_3S_4	223.3	286.6	337.6	380.3					
α-NiS	147.4	165.6	174.7	222.3	285.1	333.4	374.9		
β-NiS	143.1	178.9	206.1	221.9	244.6	283.7	297.8	349.2	370.6

Table S5. In-situ Raman spectra of $Ni_{1-x}Fe_xS_2$.

	Raman Peaks (cm^{-1})						
x = 0, 0.4 V	273.4	287.7	480.5				
x = 0, 0.3 V	273.3	287.3	480.5				
x = 0, 0.2 V	273.1	286.1	478.2				
x = 0, 0.1 V	271.8	284.5	476.5				
x = 0, 0.05 V	184.6	197.3	218.9	301.3	320.6	346.3	476.3
x = 0, -0.15 V	182.5	197.3	218.2	300.6	320.6	346.2	
x = 0, -0.25V	181.6	195.7	216.9	300.6	320.7	346.9	
x = 0.1, 0.4 V	274.2	284.9	479.8				
x = 0.1, 0.3 V	273.5	283.1	478.7				
x = 0.1, 0.2 V	270.3	281.8	476.3				
x = 0.1, 0.15 V	183.5	197.4	220.9	302.7	322.9	348.4	476.1
x = 0.1, 0.1 V	184.1	197.4	219.6	301.4	321.1	347.1	476.1
x = 0.1, -0.15 V	183.5	196.9	219.1	300.8	320.0	346.4	
x = 0.1, -0.25V	183.5	196.7	218.9	300.8	319.9	346.4	
x = 0.2, 0.4 V	273.5	285.7	479.7				
x = 0.2, 0.3 V	270.6	281.6	477.6				
x = 0.2, 0.25 V	269.6	280.6	475.7				
x = 0.2, 0.2 V	182.5	195.6	217.6	299.5	319.7	347.6	475.3
x = 0.2, 0.0 V	184.6	196.6	217.6	300.6	320.6	346.6	
x = 0.2, -0.15 V	183.6	196.6	218.6	300.6	319.5	345.6	
x = 0.2, -0.25V	183.2	196.2	218.7	299.9	321.3	346.2	
x = 0.25, 0.4 V	271.7	283.4	479.5				
x = 0.25, 0.3 V	273.4	284.2	478.3				
x = 0.25, 0.25 V	270.7	282.5	475.8				
x = 0.25, 0.2 V	185.8	197.5	218.4	300.6	320.4	347.5	475.6
x = 0.25, 0.0 V	183.0	196.6	218.4	301.5	320.5	347.4	477.6
x = 0.25, -0.15 V	180.9	195.7	217.5	300.9	318.4	345.7	
x = 0.25, -0.25V	181.0	195.6	216.0	298.7	319.0	345.7	
x = 0.33, 0.4 V	273.7	283.8	478.9				
x = 0.33, 0.3 V	271.8	283.8	477.8				
x = 0.33, 0.25 V	270.7	280.7	476.8				
x = 0.33, 0.2 V	181.8	197.8	219.8	300.6	321.4	345.7	476.4
x = 0.33, 0.0 V	186.5	198.9	220.2	300.6	322.5	349.7	
x = 0.33, -0.15 V	185.3	198.5	220.6	300.1	323.3	347.9	
x = 0.33, -0.25V	184.9	198.5	219.4	302.5	322.2	347.8	

Table S6. Comparisons of HER activity for $Ni_{1-x}Fe_xS_2$ (x = 0.0, 0.1, 0.2, 0.25 and 0.33).

	Overpotential (mV) @ 10 mA cm^{-2}	TOF (H_2 s^{-1}) @ 200 mV	Mass activity (A g^{-1}) @ 200 mV	R_{ct} (Ω) @ 150 mV
x = 0	241	0.007	11.21	45.6
x = 0.1	198	0.037	52.45	31.4
x = 0.2	121	0.136	171.09	9.8
x = 0.25	146	0.071	84.56	12.7
x = 0.33	163	0.030	31.79	18.5

Table S7. The DFT + *U* calculated energy of Ni 3*d* band center and S 3*p* band center of $Ni_{1-x}Fe_xS_2$ (x = 0.0, 0.1, 0.2 and 0.33) and FeS_2 relative to Fermi level.

	Ni 3*d* (eV)	Fe 3*d* (eV)	S 3*p* (eV)	|Ni 3*d* - S 3*p*| (eV)	|Fe 3*d* - S 3*p*| (eV)
x = 0.0	-4.655		-2.638	2.017	
x = 0.1	-4.542	-2.504	-2.573	1.969	0.069
x = 0.2	-4.298	-1.885	-2.357	1.941	0.472
x = 0.33	-4.027	-1.447	-2.455	1.572	1.008
FeS_2		-1.315	-2.777		1.462

Table S8. The sulphur vacancy formation enthalpy ΔHf, Vs of $Ni_{1-x}Fe_xS_2$ (x = 0.0, 0.1, 0.2 and 0.33) and FeS_2 from DFT + U calculation.

	Energy (eV)	μ_i (eV)	ΔHf, Vs (eV)
NiS_2	-233.93		
NiS_2 - V_S	-228.62	-4.12	1.19
$Ni_{0.9}Fe_{0.1}S_2$	-238.94		
$Ni_{0.8}Fe_{0.2}S_2$ - V_S	-234.03	-4.12	0.79
$Ni_{0.8}Fe_{0.2}S_2$	-243.73		
$Ni_{0.8}Fe_{0.2}S_2$ - V_S	-238.93	-4.12	0.68
$Ni_{0.67}Fe_{0.33}S_2$	-249.46		
$Ni_{0.67}Fe_{0.33}S_2$ - V_S	-244.28	-4.12	1.06
FeS_2	-321.14		
FeS_2 - V_S	-314.28	-4.12	2.74

Table S9. The values of ΔG_{H^*} of H* at stable adsorption sites Ni_3S_2 slab and Fe doped Ni_3S_2 slab.

	Slab (eV)	Slab-H (eV)	Correction (eV)	ΔG_{H^*} (eV)
Ni_3S_2	-195.793	-198.430	0.218	0.981
8.3% Fe-Ni_3S_2	-198.986	-202.264	0.215	0.336
16.7% Fe-Ni_3S_2	-202.848	-206.383	0.226	0.091
25.0% Fe-Ni_3S_2	-206.341	-210.045	0.214	-0.090
33.3% Fe-Ni_3S_2	-210.059	-213.544	0.216	0.131

Table S10. The formation energy of $Ni_{1-x}Fe_xS_2$ (x = 0.0 and 0.2) for reconstruction.

Structure	NiS_2	Ni_3S_2	V_S-20%Fe@NiS_2	S	20%Fe@Ni_3S_2
Formula	Ni_4S_8	Ni_9S_6	$Fe_4Ni_{16}S_{39}$	S_{32}	$Fe_9Ni_{36}S_{30}$
Energy (eV)	-58.207	-80.422	-299.336	-131.949	-422.593
Normalization (eV)	-14.552	-26.807	-14.967	-4.123	-28.173
Formation Energy (eV)		0.059 eV (E_{f1})	0.040 eV (E_{f2})		

$NiS_2 = 1/3\ Ni_3S_2 + 4/3\ S$ (1)

$E_{f1}' = 1/3\ E\ (Ni_3S_2) + 4/3\ E(S) - E\ (NiS_2) = 0.118$ eV

$E_{f1} = 0.059$ eV

V_S-$Fe_{0.2}Ni_{0.8}S_2 = 1/3\ (Fe_{0.2}Ni_{0.8})_3S_2 + 4/3\ S$ (2)

$E_{f2}' = 1/3\ E(20\%Fe@Ni_3S_2) + 4/3\ E(S) - E(V_S\text{-}20\%Fe@NiS_2) = 0.080$ eV

$E_{f2} = 0.040$ eV

The formation energy is a value normalized to NiS_2 or $Fe_{0.2}Ni_{0.8}S_2$. For convenience of expression, the result normalized to a single sulphur atom as $E_{fn} = E_{fn}'/2$.

Operando XAFS experiment at Fe K-edge illustrated that $Fe_{0.2}Ni_{0.8}S_2$ displayed a reconstruction process with the distorted Fe tetrahedral structure. Moreover, in-situ Raman and operando Ni K-edge XAFS characterizations (Fig. 3a and Fig. 4a in manuscript) demonstrated that $Ni_{0.8}Fe_{0.2}S_2$ catalysts presented a phase transformation into the heazlewoodite-type Ni_3S_2 structure with Ni-S_4 coordination. Considering these reconstructed results for $Ni_{0.8}Fe_{0.2}S_2$ catalysts comprehensively, the state of Fe after the reconstruction in $Ni_{0.8}Fe_{0.2}S_2$ catalysts were Fe doped Ni_3S_2. Moreover, sulfur vacancies were demonstrated in the $Ni_{0.8}Fe_{0.2}S_2$ catalysts by XAFS results (Table S1). On the basis, the reconstruction process was discussed in two cases. The first case was the generating of Ni_3S_2 from the phase transition of NiS_2. The second case was the generating of 20% Fe doped Ni_3S_2 from the phase transition of V_S-20%Fe@NiS_2 (considering sulphur vacancies in 20%Fe doped-NiS_2), and the detailed calculation process was illustrated in Equation 1 and Equation 2.

The formation energy of the reconstruction process was calculated and the results demonstrated a smaller barrier ($E_{f2} < E_{f1}$) for the phase transformation of Fe substituted nickel sulfides from the pre-structure to the finalized structure, which theoretically supported the experimental results that Fe substitution prompted the reconstruction process.

Table S11. In-situ Raman spectra of α-NiS, β-NiS and Ni_3S_4.

	Raman Peaks (cm^{-1})						
β - NiS, 0.4 V	147.9	169.4	228.2	244.9	298.7	349.1	369.1
β - NiS, 0.2 V	144.5	168.9	225.0	243.7	297.6	346.8	368.1
β - NiS, 0.15 V	139.7	171.4	221.5	242.6	295.3	346.8	366.4
β - NiS, 0.1 V	181.8	195.8	218.0	300.0	321.1	345.6	
β - NiS, -0.15 V	185.2	196.9	218.0	301.1	322.2	347.8	
β - NiS, -0.25 V	182.9	195.8	217.9	298.7	321.1	345.5	
α - NiS, 0.4 V	164.3	175.7	221.5	285.7	348.5		
α - NiS, 0.2 V	175.5	220.9	284.4	347.9			
α - NiS, 0.1 V	165.8	220.2	283.0	347.2			
α - NiS, 0.05 V	182.5	196.5	218.7	301.2	322.0	348.5	
α - NiS, -0.15 V	181.2	197.8	220.2	301.1	320.7	347.2	
α - NiS, -0.25 V	183.8	198.0	220.2	302.5	320.7	347.2	
Ni_3S_4, 0.4 V	223.1	286.1	339.7	381.6	477.2		
Ni_3S_4, 0.2 V	220.1	283.9	334.3	376.8	476.4		
Ni_3S_4, 0.1 V	220.1	283.7	336.7	379.1	477.3		
Ni_3S_4, 0.05 V	186.7	199.6	221.4	303.6	323.3	349.2	
Ni_3S_4, -0.15 V	181.4	195.5	216.1	299.2	320.4	345.1	
Ni_3S_4, -0.25 V	181.9	195.5	217.3	299.2	319.8	345.1	

Supplementary Note 1. The discussion on the DFT results of H adsorption and water activation process on the real active structure.

The (101) slab of Fe-doped Ni_3S_2 was built to evaluate the HER activity according to the in-situ Raman and TEM results (Figure S22a). With the increment of Fe doping amount, the surface become chaotic, and S atoms gradually run to the outermost layer. In Figure S22b, the electron-density isosurface distribution shows that S is easy to accept electrophilic reagents (H atoms) to adsorb, and this can be confirmed by the in-situ Raman in Figure S18. DFT results in Figure S22c display that Fe substitution can decrease the ΔG_{H^*} from 0.981 eV to -0.091 eV when the doping amount of Fe reached 25 %, and the further incremental Fe substitution amount (33.3%) enhanced the ΔG_{H^*} to 0.131 eV. The calculated results are consistent with our experimental results that 20% (16.7% ~25%) Fe doped nickel sulfides exhibit the best HER activity.

In addition, the water adsorption and dissociation behavior on the electrocatalyst surface as the same initial step for HER is a crucial factor for water splitting in basic electrolyte. The H-O-H bond must first be destroyed by the dissociation of water prior to the adsorption of H*, (i.e., $H_2O + e^- \rightarrow H^* + OH^-$ [the Volmer reaction]). The calculated results illustrate that water adsorption is more thermodynamically favorable on Fe doped Ni_3S_2 (Figure S22d, f). Specifically, the water adsorption free energies (E_{ads}, -0.510 eV) of Fe doped Ni_3S_2 on Fe site own the lowest, suggesting that water adsorption on Fe site of Fe doped Ni_3S_2 is easier than those on Ni site of Fe doped Ni_3S_2 and Ni_3S_2 (E_{ads} is -0.234 and -0.019 eV, respectively). It should be noted that there is also a much lower energy barrier for water dissociation in the catalytic Fe doped Ni_3S_2 from the DFT results (Figure S22e, g), which collaboratively favor the Volmer step to generate H_{ads}. Unfortunately, Ni_3S_2 exhibits unfavorable catalyst-OH_{ad} energetics on the Ni site, exhibiting a very high activated water adsorption energy $\Delta G(H_2O)$ up to 1.309 eV. This high $\Delta G(H_2O)$ significantly hinders the dissociation of water to H* intermediates and leads to sluggish HER kinetics. Notably, Fe doped Ni_3S_2 electrocatalysts can provide the active sites for hydroxyl adsorption, and the followed $\Delta G(H_2O)$ is reduced to 0.159 eV on the Fe site of Fe doped Ni_3S_2, indicating the Fe doped Ni_3S_2 electrocatalysts are effective for cleaving HO–H bonds.

Based on these, Fe substitution in nickel sulfides can efficiently promote water adsorption and activation process to facilitate the Volmer step to optimize H adsorption. Fe substitution can also vary the electronic structure of catalyst to modulate S−H_{ads} bonds formed on catalyst surfaces and will optimize H desorption to promote Heyrovsky step to realize efficient performance in alkaline media.

Supplementary Note 2. The discussion on the dynamic reconstruction process of Fe doped α-NiS, β-NiS and Ni_3S_4.

XRD patterns and XAFS results in Figure S24 demonstrate that the as-prepared β-$Ni_{1-x}Fe_xS$ catalysts maintain the rhombohedral crystal structure (JCPDS 12-0041), and Fe substitution suggests a great flexibility in β-$Ni_{1-x}Fe_xS$ catalysts with a lower Ni valence state, more sulphur vacancies and the increased lattice disorder. In Figure S25, in-situ Raman results present that Fe doping can facilitate the reconstruction process of β-NiS catalysts with the reconstruction potential thresholds locating in regions of 0.15~0.1 V, 0.15~0.1 V, and 0.2~0.15 V (vs. RHE) for x = 0, 0.05 and 0.1, respectively. Notably, β-$Ni_{0.9}Fe_{0.1}S$ electrode displays superior HER activity with an overpotential of 189 mV at 10 mA cm^{-2}, Tafel slope of 55 mV dec^{-1} and the smallest R_{ct} value of 14 Ω. In Figure S25f, the exhibited synchronous trend between reconstruction potential threshold range and overpotential implicate the close correlation concerning reconstruction initiate and HER activation. Partial Fe substitution in β-NiS catalysts grants controllable sulphur vacancies to make it easier to evolve into active phase, thereby lowering the applied potential threshold for phase variation. Such phase reconfiguration enables easier activity triggering and hence optimizes HER performance. Operando XAFS in Figure S26 further demonstrate that Fe doping in β-NiS can promote the reconstruction process from a facilitated variation in the valence state of the Ni moieties as reflected by the XANES results and the reconfiguration in their local atomic structure. Specifically, the Ni-S peaks in the FT curves show an obvious low-R shift from 1.87 Å to 1.75 Å, and the FT peak's intensity exhibits a decrease for the x = 0.1 sample at -0.2 V (vs. RHE) (Figure S26d). In addition, the as-prepared $Ni_{3-3x}Fe_{3x}S_4$ and α-$Ni_{1-x}Fe_xS$ catalysts present the similar synchronous trend between reconstruction potential threshold range and overpotential with the increase of Fe doping amount, these results reconfirm the Fe substitution effect on the reconfiguration process for nickel sulfide catalysts (Figure S27 and Figure S28).

These results establish the promotion effect on phase reconfiguration process and the subsequent HER performance originated from Fe substitution, and the evolution law on transition metal's valence state, along with the dynamic structure-activity correlation have been also identified. Therefore, a universal rule of Fe substitution in multivalent transition metals-based catalysts have been demonstrated, to improve the structural flexibility, facilitating the evolution process with enhance HER performance.